



A heuristic approach to boost the performance and Cr poisoning tolerance of solid oxide fuel cell cathode by robust multi-doped ceria coating

Hafiz Ahmad Ishfaq^{a,b}, Muhammad Zubair Khan^{c,*}, Yogita Manikrao Shirke^d, Sanaullah Qamar^{d,e}, Amjad Hussain^{d,e}, Muhammad Taqi Mehran^f, Rak-Hyun Song^{d,e}, Mohsin Saleem^{f,g}

^a Department of Materials Chemistry, National Institute of Chemistry, Hajdrihova 19, 1000 Ljubljana, Slovenia

^b Faculty of Chemistry and Chemical Technology, University of Ljubljana, Večna pot 113, 1000 Ljubljana, Slovenia

^c Department of Materials Science & Engineering, Pak-Austria Fachhochschule: Institute of Applied Sciences and Technology, Mang, Haripur 22621, KPK, Pakistan

^d Department of Advanced Energy and System Engineering, Korea University of Science and Technology (UST), 217 Gajeong-ro, Yuseong-gu, Daejeon 34113, Republic of Korea

^e High-Temperature Energy Conversion Laboratory, Korea Institute of Energy Research, 152 Gajeong-ro, Yuseong-gu, Daejeon 34129, Republic of Korea

^f School of Chemical and Materials Engineering (SCME), National University of Sciences & Technology (NUST), H-12, Islamabad 44000, Pakistan

^g School of Interdisciplinary Engineering & Sciences, National University of Sciences & Technology (NUST), H-12, Islamabad 44000, Pakistan



ARTICLE INFO

Keywords:

Solid oxide fuel cell
Cathode
Oxygen reduction reaction
Performance
Cr-poisoning

ABSTRACT

Herein, highly conductive, robust, and innovative Gd and Pr multi-doped ceria (GPDC) coating, to boost the ORR kinetics and stability against Cr poisoning of the state-of-the-art $\text{La}_{0.6}\text{Sr}_{0.4}\text{Co}_{0.2}\text{Fe}_{0.8}\text{O}_{3-\delta}$ (LSCF) cathode, is reported. The GPDC coating significantly enhanced the ORR kinetics by ameliorating the surface of the LSCF cathode and showed a two-fold increment in the electrochemical performance compared to the cell with a bare LSCF cathode. The SOFC with GPDC-coated LSCF cathode showed outstanding stability at 700 °C for 500 h with a degradation rate of 0.001% h⁻¹ in an accelerated Cr poisoning test which is attributed to the alleviation of the formation in SrCrO_4 . Both distributions of relaxation time-based analysis and experimental results indicate that the GPDC coating improves the ORR activity and Cr tolerance of the LSCF cathode. This study provides a comprehensive and smart strategy to tailor the surface of SOFC cathode materials to enhance performance and durability.

1. Introduction

Solid oxide fuel cells (SOFCs) are highly efficient electrochemical devices that directly convert chemical energy stored in hydrocarbon fuel to electrical energy. SOFCs gaining enormous attention in recent years due to their higher efficiency, remarkable fuel diversification, and green nature [1–3]. From a commercialization point of view, SOFC technology requires substantial improvement to economically compete with established combustion-based energy conversion technologies due to its high-temperature operation and shorter lifetime [4,5]. Lowering the operating temperature from high temperatures (HT; 800 – 1000 °C) to intermediate temperatures (IT; <750 °C) is the viable solution to bring this technology into the market. This will allow the utilization of relatively inexpensive materials (e.g., ferritic stainless steels for interconnects), minimizing the sealing problems and cell degradation

during prolonged operation [6,7]. However, the major drawback of the IT temperature operation is that the oxygen reduction reaction (ORR) kinetics at the SOFC oxygen electrode becomes extremely sluggish [8,9]. Therefore, systematic research on developing new materials and increasing the electrocatalytic activity of existing cathode materials at intermediate temperature ranges is considered a consensus for the practical application of IT-SOFCs.

Over the past decades, several mixed ionic and electronic conductor (MIEC) cathode materials such as $\text{La}_{0.6}\text{Sr}_{0.4}\text{Co}_{0.2}\text{Fe}_{0.8}\text{O}_{3-\delta}$ (LSCF) have been widely studied as a high-performance cathode material for IT-SOFCs [10–12]. Nevertheless, at reduced temperatures, LSCF has sluggish kinetics for oxygen transport because of its high activation energy (186 kJ mol⁻¹ [13]) for O^{2-} diffusion and low oxide ionic conductivity (1×10^{-2} S cm⁻¹ at 700 °C [14]). This reflects that the kinetics of the oxygen surface exchange reaction, which is the rate-determining step for

* Corresponding author.

E-mail address: zubair.khan@fcm3.paf-iast.edu.pk (M.Z. Khan).

ORR, on the LSCF cathode still demands extensive improvement to enhance the electrochemical performance of IT-SOFCs [15]. To address this issue, usually, LSCF is combined with highly ionic conductive oxides such as gadolinia doped ceria (GDC; $\text{Gd}_x\text{Ce}_{1-x}\text{O}_{2-x/2}$) or samarium doped ceria (SDC; $\text{Sm}_x\text{Ce}_{1-x}\text{O}_{2-x/2}$) to boost the kinetics of ORR of the LSCF cathode [16–18]. In addition to that, LSCF-based cathode reacts with rare earth (Y, Sc, etc.) stabilized zirconia and leads to the formation of an insulating phase (such as SrZrO_3 and $\text{La}_2\text{Zr}_2\text{O}_7$) near the cathode/electrolyte interface [12,19]. Generally, the GDC interlayer is inserted between the cathode and electrolyte to prevent the formation of such insulating phases, however, GDC may increase the interfacial resistance of the cell [20,21]. Therefore, replacing GDC with a higher ionic conducting electrolyte is reported to reduce the interfacial polarization resistance [22]. As doping the ceria with multiple cations is one of the promising approaches to significantly enhance the ionic conductivity of ceria-based oxides [23,24]. Consequently, the increased ionic conductivity of doped ceria leads to the enhancement in the ORR kinetics of the LSCF cathode [6,25]. Based on the density functional theory modeling, Andersson et al. [26] reported that an optimized balance between attractive electronic and repulsive elastic contributions can increase the ionic conductivity of ceria-based materials. This can be achieved by doping the ceria-based materials with a combination of trivalent cations with atomic numbers between 61 (Pm) and 62 (Sm). Moreover, Omar et al. [27] reported that the ionic conductivity of Sm- and Nd multi-doped ceria (SNDC) is 30% higher than the GDC, making it a potential electrolyte as well as electrode material for the SOFCs. In coherence with this, Tuller et al. [28] have investigated the $\text{Pr}_x\text{Ce}_{1-x}\text{O}_{2-\delta}$ (PCO) system and revealed that PCO exhibit several interesting features related to the ability of the Pr ion to reduce under relatively oxidizing conditions and can be used as the cathode material for the SOFC. However, the effect of Pr-doped materials, as active components in SOFCs cathodes, on the electrochemical performance of SOFCs has been rarely reported.

The poor surface stability of LSCF due to excessive surface segregation of Sr/SrO is another major technical barrier that limits its broader application [29,30]. Practically, Cr-containing steel interconnects are used to stack multiple SOFCs in series to get high voltage [31]. At elevated temperatures and humid atmospheres, the Cr species such as CrO_3 and Cr(OH)_2 from the interconnect react with the surface segregated SrO to form insulating phases (e.g., SrCrO_4 and Cr_2O_3) on the LSCF surface and deteriorate the ORR electrocatalytic activity of the LSCF cathode [32]. Thus, there is a pressing appeal to tailor the surface of the LSCF with catalyst coatings to mitigate the Cr-poisoning effect while enhancing the ORR activity during the prolonged operation. Therefore, the use of a Sr-free catalyst is one of the promising strategies to enhance LSCF stability [33,34]. In contribution to this, Zhao et al. [35] have compared the Cr deposition and poisoning on $\text{La}_{0.8}\text{Sr}_{0.2}\text{Ga}_{0.8}\text{Mg}_{0.2}\text{O}_{3-\delta}$ (LSGM) and GDC electrolyte materials and found that GDC, as a Sr-free oxide material, promises higher Cr tolerance in contrast to LSGM. Similarly, San Ping Jiang group [36] coated the surface of LSCF with GDC catalysts and their results revealed the outstanding stability of the LSCF cathode against a Cr-containing atmosphere.

Inspired by these developments, herein, we report novel multi-doped ceria with trivalent praseodymium (Pr^{3+}) and gadolinium (Gd^{3+}) cations with a chemical composition of $\text{Gd}_{0.1}\text{Pr}_{0.1}\text{Ce}_{0.8}\text{O}_{2-\delta}$ (GPDC) which exhibits the significantly enhanced ionic conductivities than GDC. For the first time using this multi-doped ceria, we tailored the surface of the LSCF cathode by coating it with GPDC catalysts via the wet impregnation method [37,38]. The GPDC-coated LSCF cathode showed excellent improvement in the ORR electrocatalytic activity of LSCF by boosting the oxygen surface exchange reaction on the LSCF surface. Importantly, the GPDC-coated LSCF cathode showed impressive tolerance against stringent Cr and H_2O -containing atmospheres with slight degradation rates of $0.001\% \text{ h}^{-1}$ in anode-supported SOFCs attributed to the alleviation in the SrCrO_4 formation.

2. Materials and methods

2.1. Preparation of GPDC powders and pellets

Gd and Pr multi-doped ceria (GPDC) with a nominal composition of $\text{Gd}_{0.2-x}\text{Pr}_x\text{Ce}_{0.8}\text{O}_{2-\delta}$ ($x = 0, 0.02, 0.04, 0.06, 0.08, 0.1$, and 0.15) were synthesized by a sol-gel method [39]. Stoichiometric amounts of $\text{Gd}(\text{NO}_3)_3 \cdot 6\text{H}_2\text{O}$ (99.9% Sigma-Aldrich), $\text{Pr}(\text{NO}_3)_3 \cdot 6\text{H}_2\text{O}$ (99.9% Sigma-Aldrich), and $\text{Ce}(\text{NO}_3)_3 \cdot 6\text{H}_2\text{O}$ (99.9% Sigma-Aldrich) were dissolved in de-ionized water, and magnetically stirred at room temperature until the solution became clear. Citric acid monohydrate ($\text{C}_6\text{H}_6\text{O}_7 \cdot \text{H}_2\text{O}$) was added with metal to a citric acid molar ratio of 1:2 and the temperature was increased to 80°C . Ethylene glycol was added at a 1:2 molar ratio (citric acid to ethylene glycol) and stirred in the solution until a viscous gel was formed. The resulting gel was heated at 250°C and subsequently calcined at 1000°C for 5 h. The obtained powder was then ball milled for 24 h in ethanol, dried overnight in the oven at 100°C , and the resulting GPDC powder was granulated by sieving. The prepared GPDC powders were uniaxially pressed at 50 MPa followed by sintering at 1400°C for 5 h to form the dense pellets for total (ionic and electrical) conductivity measurements via the four-probe method [40].

2.2. Fabrication of symmetric cells

Symmetric cells composed of LSCF/GDC/LSCF were prepared by fabricating a dense GDC electrolyte substrate by uniaxial pressing of GDC powder (Fuel Cell Materials, USA) at ~ 2 metric tons. The green disk shape GDC pellets were then sintered at 1400°C in the air for 10 h. The final thickness of the GDC pellets was around $1\ \mu\text{m}$ after the sintering. The cathode paste was prepared by mixing the LSCF powder (Fuel Cell Materials, USA) with ink vehicle (Fuel Cell Materials, USA) in a 2:1 quantity at 1500 rpm for 10 min. Prepared cathode paste was screen printed on both sides of the dense GDC disk and fired at 1025°C for 3 h in the air. A platinum (Pt) reference electrode was attached to the surface of the GDC electrolyte to decouple the LSCF electrode contribution from the whole cell. The prepared LSCF electrodes had an effective area of $0.5\ \text{cm}^2$ and a thickness of $\sim 30\ \mu\text{m}$.

2.3. Preparation and process of GPDC infiltration solution

The GPDC infiltration solution was prepared by adding stoichiometric amounts of $\text{Gd}(\text{NO}_3)_3 \cdot 6\text{H}_2\text{O}$ (99.9% Sigma-Aldrich), $\text{Pr}(\text{NO}_3)_3 \cdot 6\text{H}_2\text{O}$ (99.9% Sigma-Aldrich), $\text{Ce}(\text{NO}_3)_3 \cdot 6\text{H}_2\text{O}$ (99.9% Sigma-Aldrich), and urea in a mixture of a solvent consisting of 55 vol% deionized water and 45 vol% ethanol to form 1 M solutions. The urea-to-cation ratio (U/C) was fixed at 10 which acts as a surfactant to form the desired GPDC ($\text{Gd}_{0.1}\text{Pr}_{0.1}\text{Ce}_{0.8}\text{O}_{2-\delta}$) phase at low temperatures. The solution was magnetically stirred at 300 rpm at 50°C until the complete dissolution of nitrates. A $3\ \mu\text{l}$ of prepared GPDC solution was impregnated into the porous LSCF cathode by using the micro-syringe yielding the solution loading of $1\ \text{mg}/\text{cm}^2$, followed by drying at 100°C for 2 h. In a similar way, porous LSCF cathodes were infiltrated two, three, and four times to get the solution loading of 2, 3, and $4\ \text{mg}/\text{cm}^2$ respectively, with an intermediate drying step at 100°C .

The experimental details of the weight changes during infiltration, GPDC loading, and the required amount of GPDC solution are described in Table S1 (Supplementary Data). The GPDC-infiltrated porous LSCF cathodes were calcined at 850°C for 1 h to form the GPDC phase. The entire process of GPDC coating with different infiltration cycles is schematically shown in Fig. 1.

2.4. Fabrication of anode-supported SOFC

The slurries of anode support, anode functional layer (AFL), and electrolyte were prepared by mixing NiO (J. T. Baker)- 8 mol.% Y_2O_3 -

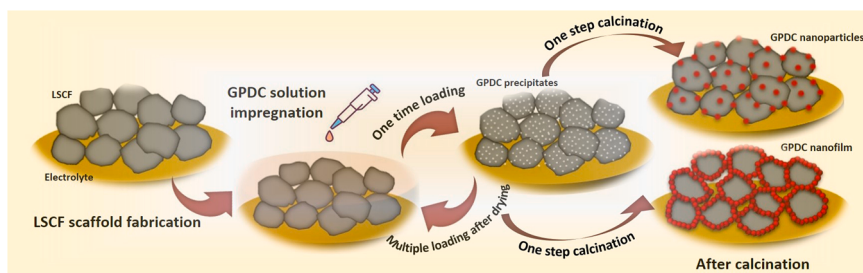


Fig. 1. Schematic illustration of the experimental steps involved in GPDC coating on LSCF cathode via wet infiltration method. The GPDC nanofilm was obtained at high catalyst loading.

stabilized-ZrO₂ (8YSZ) powder, NiO- (Sc₂O₃)_{0.10}(CeO₂)_{0.01}(ZrO₂)_{0.89} (ScCeSZ; Fuel Cell Materials, USA), and ScCeSZ powders with a suitable amount of commercial binder (PVB79) and dibutyl-phthalate (DBP) plasticizer, respectively. Each of the binder and plasticizer added anode, AFL, and electrolyte powders were separately mixed by a ball-milling process for 24 h with toluene and isopropyl alcohol (IPA). Triton-X and fish oil were also added to the mixture as a surfactant and as a dispersant, respectively for the formation of a homogenous slurry. After ball milling, slurries were degassed for 10 mins to remove the trapped air bubbles during mixing. The tape casting was performed by which the slurries were coated onto a Si-coated polyethylene (PET) carrier at 50 °C. The anode support, AFL, and electrolyte green film were hot-laminated and finally pressed by using a warm isostatic press (WIP) with dimensions of 15 cm × 15 cm. The pressed hot films were subjected to organic burnt-out and co-sintered at 1400 °C for 5 h. The cells were cut using waterjet cutting in the form of coins or disks of 2.5 cm in diameter. The GDC (Fuel Cell Materials, USA) diffusion barrier layer was screen-printed on the top of the ScCeSZ electrolyte, and sintering was performed at 1250 °C in the air for 3 h. The LSCF (Fuel Cell Materials, USA) electrode was screen-printed onto the sintered GDC layer and then sintering was done at 1025 °C for 3 h in air. GPDC-coated LSCF electrodes were prepared similarly as described in Section 2.3. by keeping the GPDC loading to 3.0 mg/cm².

2.5. Materials and electrochemical characterization

The identification of the phase and crystallographic structure of electrodes and prepared powders were done by X-ray diffraction (XRD, 2500 D/MAX, Rigaku). The refinement and phase analysis of the XRD pattern of prepared GPDC powders and infiltrated electrodes was accomplished by using full-proof software. The morphologies and microstructures of the cell constituent layers were analyzed by using a scanning electron microscope (SEM, Hitachi Sue8230) and transmission electron spectroscopy (TEM, Talos F200X) coupled with energy dispersive spectroscopy (EDS) for elemental analysis. X-ray photoelectron spectroscopy (XPS, Thermo Multi-Lab 2000 spectrometer) was used to analyze the elemental oxidation states of cations and surface oxygen vacancies. The Raman spectra were measured by using surface-enhanced Raman spectroscopy in the range of 200–1400 cm⁻¹ on dense LSCF and GPDC-coated LSCF pellets. For this purpose, bare LSCF dense pellets were fabricated by uniaxial pressing of LSCF powders (Fuel Cell Materials, USA) at 50 MPa followed by sintering at 1400 °C for 5 h. The GPDC-coated LSCF pellets were prepared by dropping 9 µl of GPDC infiltration solution on the top of dense LSCF pellet followed by drying (100 °C for 2 h) and calcination (850 °C for 1 h) steps. We have used the Crofer 22 APU mesh (coated with Cr₂O₃, as a Cr source) and Ag wires attached to these pellets with Ag paste to apply the current. Fig. S9 a (Supplementary Data) schematically illustrates the elementary steps involved for the SERS on bare and GPDC-coated LSCF samples.

The conductivity (σ) of sintered GPDC pellets with different Pr concentrations was investigated using a potentiostat (VMP3, BioLogic). For this purpose, the electrochemical impedance spectroscopy (EIS)

spectra were recorded in the air at a frequency range of 1–1 mHz and different temperatures of 550, 600, 650, 700, and 750 °C by using Ag meshes and wires as current collectors attached to the pellets using Ag paste. The σ of prepared pellets was calculated by using the following equation [41]:

$$\sigma = \frac{d}{A \times R} \quad (1)$$

where d is the thickness, A is the area, and R is the measured resistance of the GPDC pellets, respectively.

The electrochemical performance of the anode-supported SOFCs was examined by measuring current density-voltage (I-V) polarization curves and EIS spectra while supplying humidified hydrogen (3 vol% H₂O) as fuel and air as an oxidant. The EIS of reference (without infiltration) cells and infiltrated cells was performed with an AC amplitude of 14 mV over a frequency range of 1 kHz – 1 mHz under open-circuit voltage (OCV) conditions at 600, 650, and 700 °C. Both the EIS spectra and current density-voltage (I-V) polarization curves were recorded by using a potentiostat (SP240, BioLogic). The EIS spectra were fitted with the Scribner Z-view software. An accelerated Cr-poisoning atmosphere was created in both symmetric and full cells by applying a Crofer 22 APU mesh pasted with Cr₂O₃ paste towards the oxygen electrode and supplying humidified air to promote the Cr evaporation at a high operating temperature. Fig. 5g schematically illustrates the Cr poisoning source for the SOFC testing. More details about the Cr-poisoning test can be found in the previous work done by our group [42].

3. Results and discussion

3.1. Phase characterization and optimization of GPDC composition

Fig. 2(a) shows the XRD spectra of prepared GPDC (Gd_{0.2-x}Pr_xCe_{0.8}O_{2-δ}; x = 0, 0.02, 0.04, 0.06, 0.08, 0.1, and 0.15) powders with different concentrations of Pr dopant. The XRD spectrum of GPDC with zero mol.% of dopant corresponds to the spectrum of the pure GDC. The prepared GDC powder shows the formation of cubic fluorite structure and the results match well with the reported data in the literature [43]. All the peaks are shifted towards lower angles when the GDC is doped with Pr with different concentrations revealing the increase in the lattice constant as shown in Fig. 2(a) and Fig. S1a (Supplementary Data). This is due to the replacement of smaller Gd³⁺ (1.053 Å) with larger Pr³⁺ (1.126 Å) cations [44]. The conductivity of prepared GPDC pellets with different Pr-dopant concentrations was analyzed by measuring the EIS spectra and the results are summarized in Fig. 2(b). According to Fig. 2(b), the σ of GPDC with a Pr concentration of 10 mol.% showed the maximum ionic conductivity at all temperatures among other dopant concentrations. For instance, the GDC showed a σ of 0.037 Scm⁻¹ at 700 °C which increased to 0.053 Scm⁻¹ at 10 mol.% dopant concentration. This increase is ~43% compared to that of pure GDC. However, GPDC σ value decreased to 0.045 Scm⁻¹ at 15 mol.% Pr dopant concentration. Based on these results, we have fixed the GPDC

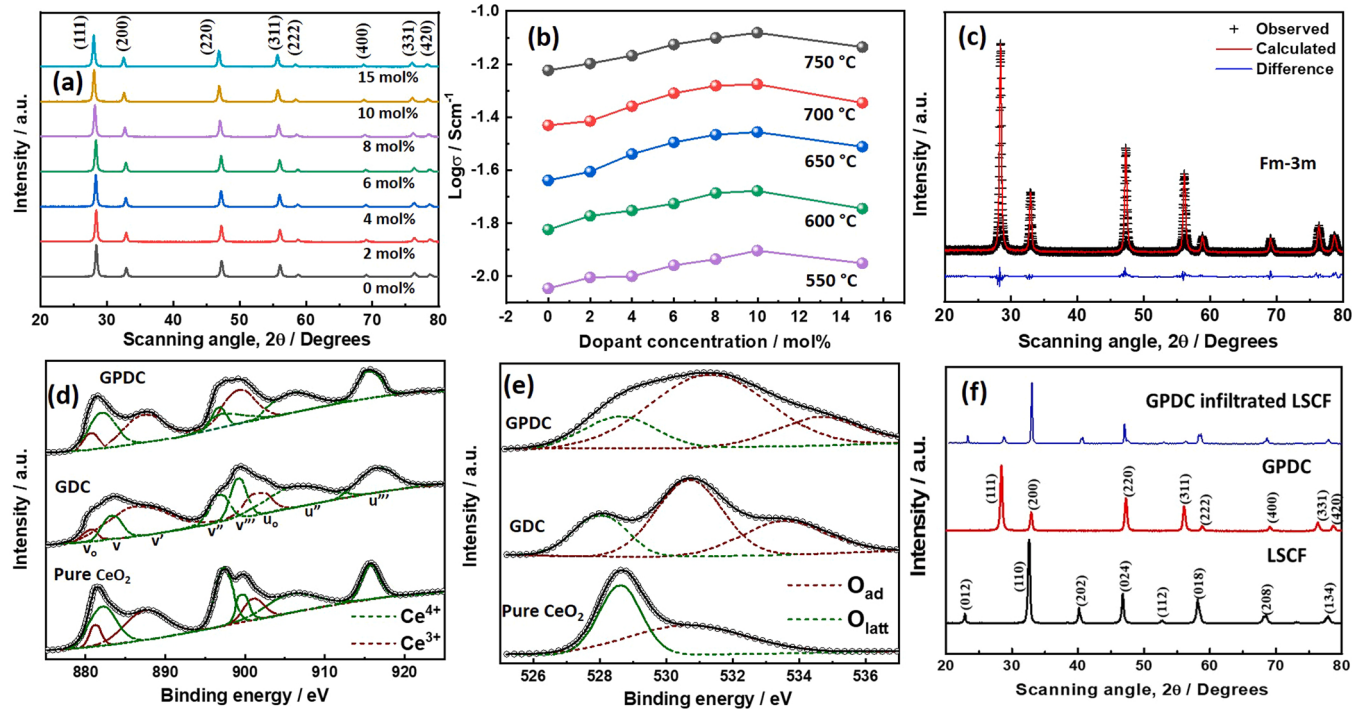


Fig. 2. (a) XRD spectra of GPDC powder with different dopant concentrations (b) The conductivity of GPDC as a function of Pr dopant concentrations at a temperature range of 550–750 °C. (c) Illustration of XRD refinement by full proof software on a GPDC with 10 mol% dopant sample. Obtained XPS spectra of (d) Ce 3d and (e) O 1s orbitals in pure CeO₂, GDC, and 10 mol.% GPDC powders (f) XRD spectra of LSCF electrode without and with 10 mol% GPDC infiltration showing good chemical compatibility with LSCF after calcination at 850 °C for 1 h.

composition of Gd_{0.1}Pr_{0.1}Ce_{0.8}O_{2-δ} in this study for further experiments. Fig. 2(c) shows an example of the XRD refinement of GPDC with a nominal composition of Gd_{0.1}Pr_{0.1}Ce_{0.8}O_{2-δ} using full-proof software. To verify the match between observed and calculated data, we used a weighted profile R-factor (R_{wp}) which is defined as the mean deviation according to the calculated data. The R_{wp} is close to 0.081 for GPDC powders suggesting that the refinement was in good agreement with the observed XRD spectrum of GPDC [45]. Based on this, the lattice parameter ‘a’, for the cubic fluorite phase for GPDC powders with different dopant concentrations was measured and the results are displayed in Fig. S1(b) (Supplementary Data). The lattice constant increased from 5.419 to 5.447 Å for the dopant concentration of 0–15 mol.%, respectively, thereby validating Vegard’s Law [46]. The increased lattice constant with increasing Pr doping concentration increases the oxygen vacancy concentration and hence, is consistent with the increasing σ with dopant concentration as shown in Fig. 2(b). However, beyond 10 mol.% dopant concentration, the σ is decreased even if it has a large ‘a’ which is due to the more defect interactions and hence has lower mobile oxygen vacancies [27]. The doping of cerium oxide (CeO₂) with lower-valent oxides, such as rare-earth oxides RE₂O₃, results in oxygen vacancies as shown in the following Kroger-Vink notation (Eq. (5)) [47].



Due to the doping, RE dopants (RE'_{Ce}) and oxygen vacancies (V_o^{y}) inevitably creates in the CeO₂ and are the dominating defects whose concentration depends on the dopant fraction which is controlled by $[\text{RE}'_{\text{Ce}}] = [2V_o^{\text{y}}]$ (i.e., one RE'_{Ce} creates two oxygen vacancies) [48]. The generated oxygen vacancies are then responsible for ionic conduction in doped ceria by the hopping mechanism. In Fig. 2(b), oxygen ion conductivity increases steeply with increasing Pr dopant fraction to a maximum at 10 mol% dopant concentration and then declines gently. Eq. (5) indicates that oxygen vacancies are responsible for the first rise in oxygen ion conductivity with increasing dopant fraction.

As dopant concentration increases, more percolation paths are formed, causing the conductivity to decrease. According to Faber et al., the decrease in conductivity is the result of attractive interactions between dopant cations and oxygen vacancies [49]. The probability of the dopant cations sitting close together increases (i.e., defect interaction) with increasing dopant concentration above 10 mol.%. As a result, ‘deep traps’ (which require high migration energy for V_o^{y} jumps) are formed that accommodate all oxygen vacancies that are currently mobile [47, 48, 50]. Therefore, the diffusion paths for mobile oxygen vacancies become more resistant, thus increasing the activation energy for ionic conduction.

To validate how multi-cation doping of ceria with Gd³⁺ and Pr³⁺ increases the oxygen vacancy concentration on the surface, we recorded the XPS spectra on GDC and GPDC powders along with pure CeO₂ as a reference to analyze the surface chemical properties. Fig. 2(d) shows the 3d orbital spectra of Ce in the pure CeO₂, GDC, and GPDC powders. These spectra were further deconvoluted into eight subpeaks. According to the literature, three peaks labeled as v_o , v' , and u_o (with brown dash lines) are related to the Ce ions in +3 state whereas the rest of the peaks (v , v' , v'' , u' , and u'' , with green dash lines) are assigned to the Ce⁴⁺ ions indicating the coexistence of Ce³⁺ and Ce⁴⁺ in all samples [51–53]. Based on the integration of the corresponding peak regions, Ce ions with +3 and +4 oxidation states were calculated for pure CeO₂, GDC, and GPDC [54]. It was found that pure CeO₂, GDC, and GPDC had relative Ce³⁺ contents of ~30.8%, 37.4%, and 45.1%, respectively. The reduction of Ce⁴⁺ to Ce³⁺ resulted in negative substitutional defects (Ce'_{ce}), which were compensated by the generation of oxygen vacancies (V_o^{y}) [55]. The higher Ce³⁺ concentration in GPDC implies the substantial formation of oxygen vacancies on the surface [54, 56]. Also, in Fig. 2(e), the O 1 s XPS core-level spectra of pure CeO₂, GDC, and GPDC show features of two different oxygen species, including chemically adsorbed oxygen species which is related to the oxygen vacancies (O_{ad} , at higher binding energy with brown dash lines) and lattice oxygen (O_{latt} , at lower binding energy with green dash lines) [54, 57, 58]. GPDC (82.7%) has a

higher oxygen vacancy ratio than GDC (77.6%) and pure CeO_2 (53.6%), which is beneficial for oxygen surface exchange reaction and conduction at the bulk level [54]. This explains why doping the CeO_2 with multi-cations of Gd^{3+} and Pr^{3+} increases the conductivity due to the significant generation of oxygen vacancies.

Fig. 2(f) shows the comparison of XRD spectra of LSCF cathodes without and with GPDC infiltration after calcination at 850 °C for 1 h. According to these results, the good chemical compatibility of GPDC with LSCF is evident. The formation of any secondary phase is not detected on LSCF after the calcination. Additionally, the peak intensities of GPDC increased as a function of GPDC loading, signifying the enhanced coverage of GPDC over the LSCF electrode backbone (Fig. S2, Supplementary Data).

3.2. Morphology and structure of GPDC infiltrated LSCF cathodes

SEM analysis was performed to evaluate the effects of different GPDC loadings onto porous LSCF cathode. It is pertinent to mention that the calcination at 850 °C was carried out only after the final cycle of GPDC infiltration. Fig. S3(a) (Supplementary Data) shows the SEM image of the bare LSCF cathode. After the GPDC loading of 1 and 2 mg/cm², GPDC forms nanoparticles onto the surface of LSCF (Fig. S3 (b) and (c), Supplementary Data). With a further increase in GPDC loading to 3 mg/cm², the GPDC nanoparticles start to occupy all the space on the surface

of the LSCF particles and form a uniform coating (Fig. S3(d), Supplementary Data). Incoherent to this, the GPDC forms a thicker layer on the LSCF particle at a loading of 4.0 mg/cm² as shown in Fig. S3(e). The high-angle annular dark-field scanning transmission electron microscopy (HAADF-STEM) with EDS elemental analysis was further employed to characterize 2.0 and 3.0 mg/cm² GPDC infiltrated LSCF sample to reveal the various morphologies of GPDC catalyst onto the LSCF electrode. Increasing the GPDC loading in this range leads to a change in morphology which is depicted in Fig. S3(c) and (d). According to Fig. 3(a), the presence of La, Sr, Co, and Fe in the electrode backbone corresponds to the presence of the LSCF phase whereas the existence of Gd, Pr, and Ce elements confirms that GPDC nanoparticles formation in the range of ~20 nm under low GPDC loading. Conversely, Fig. 3(b) reveals the presence of Gd, Pr, and Ce elements representing the formation of a continuous and uniform film of GPDC onto the LSCF particle with an approximate thickness of 18–20 nm under high loading of 3.0 mg/cm². Moreover, Fig. 3(b), STEM image with GPDC loading of 3.0 mg/cm², and Figs. S3 (d) and S5(b), SEM images with GPDC loading of 3.0 mg/cm² were also quantitatively analyzed for measurement of the mean nanoparticle size of the GPDC using Image-Pro® Plus version 6.0. The microstructural features of the aforementioned images were quantified using a procedure reported in our previous study [59]. The mean GPDC nanoparticle size from Figs. 3(b), S3(d), and S5(b) (Supplementary Data) were measured to be around 25.5 nm with a standard

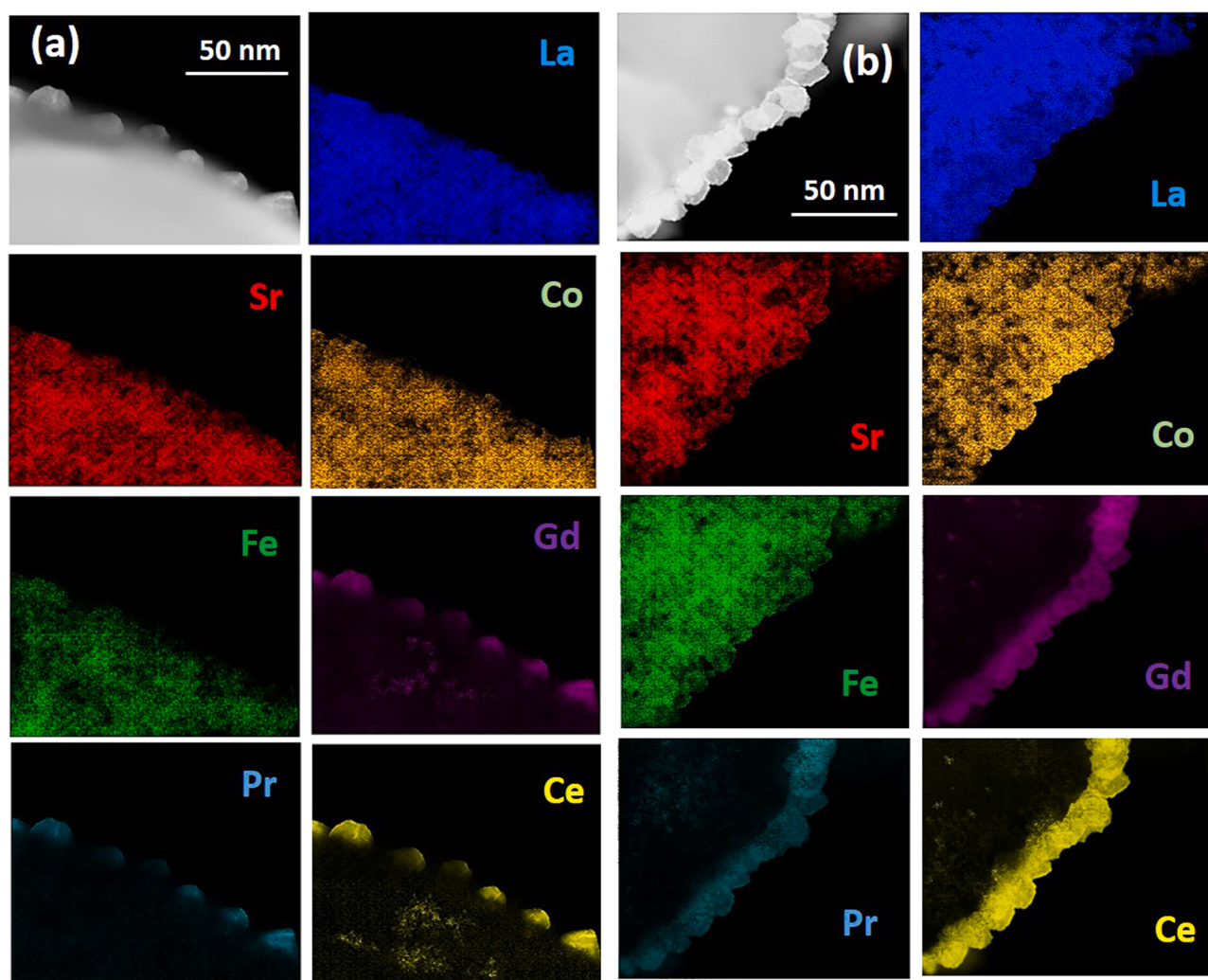


Fig. 3. HAADF-STEM EDS mapping results of GPDC infiltrated LSCF cathodes with the loading of (a) 2.0 mg/cm² and (b) 3.0 mg/cm² revealing the nanoparticle and nanofilm morphology of GPDC catalyst on LSCF, respectively.

deviation of 4.37, thereby showing better reproducibility of the infiltration process. The effect of GPDC morphology on the electrochemical performance of the SOFC will be covered in the next section.

3.3. Enhanced activity of GPDC-coated LSCF cathode

The ORR has an enormous contribution to the total impedance of the SOFCs because of its sluggish kinetics [60]. Therefore, there is a strong need to thoroughly understand the rate-determining step for the ORR on SOFC cathodic reaction. For this purpose, we used the GPDC infiltrated LSCF/GDC/LSCF symmetric cells to analyze EIS combined with DRT at different temperatures varying between 600 and 750 °C and different oxygen partial pressures ranging between 0.21 and 1.0 atm.

The samples with GPDC loading amounts of 1.0, 2.0, 3.0 and 4.0 mg/cm² are referred to as GPDC 1.0 mg/cm², GPDC 2.0 mg/cm², GPDC 3.0 mg/cm² and GPDC 4.0 mg/cm², respectively. Nyquist plots of the bare and GPDC infiltrated LSCF/GDC/GDC cells measured at 700 °C and under OCV conditions are displayed in Fig. 4(a). In the Nyquist plot, the high-frequency intercept in the real impedance axis corresponds to the ohmic resistance (R_{ohm}) of the cell and the semi-circle corresponds to the polarization resistance of the cell (R_p). In Fig. 4(a), the R_{ohm} of the cells is normalized to the origin which generally involves the resistance contribution from the electrolyte and interconnects [61]. It is important to note in Fig. 4(a) that the R_p of the GPDC infiltrated cells is significantly reduced compared to the cell with bare LSCF. The R_p of the cell with bare and LSCF cathode is 1.22 Ω.cm² which reduces to the least value of 0.35 Ω.cm² for the GPDC 3.0 mg/cm² cell. However, GPDC 4.0 mg/cm² cell showed the R_p value of 1.02 Ω.cm² at 700 °C which is indicating that increasing the GPDC loading from 3.0 to 4.0 mg/cm² leads to an increase in the R_p . A similar R_p variation trend is observed for the same samples at 750, 650, and 600 °C as shown in Fig. S4 (a-c) (Supplementary Data). The R_p of the GPDC-infiltrated LSCF electrode cells decreased as a function of GPDC loading up to 3.0 g/cm² and

increased for the loading of 4.0 g/cm².

The activation energy (E_a) of bare and GPDC infiltrated LSCF electrode cells are calculated from Arrhenius plots and presented in Fig. 4 (b). The activation energy for bare LSCF was measured to be ~1.56 eV which matches well with the reported values of 1.5–1.4 eV in the literature [62,63]. The E_a monotonically decreases to a value of ~1.39 eV with a GPDC loading of 3.0 mg/cm² which indicates better ORR activity on the GPDC-infiltrated LSCF electrodes. The decrease of E_a with increasing GPDC loading up to 3.0 mg/cm² is consistent with the R_p variation. The decrease in the R_p and E_a with GPDC catalyst loading is attributed to the enlargement of the reaction sites and ultimately showed a minimum value at for GPDC 3.0 mg/cm² where it forms a continuous nanofilm of ~20 nm on the LSCF cathode (see Fig. 3b). Nevertheless, beyond the optimal GPDC loading of 3.0 mg/cm², GPDC 4.0 mg/cm² catalysts form a thicker layer of ~40 nm on the LSCF electrode (Fig. S5, Supplementary Data). This overloaded GPDC electrocatalyst deteriorates the interfacial reactions by blocking the ORR reaction sites because of the increase in diffusion lengths for O²⁻ ions [33,64]. Furthermore, the porosity of the bare LSCF cathode, GPDC 3 mg/cm², and GPDC 4 mg/cm² cathodes shown in Fig. S5 was quantified by the 2D image analysis technique using Image-Pro® Plus version 6.0 using a procedure reported in our previous work [59]. The porosity of the bare LSCF cathode was measured to be 24.9% whereas GPDC 3.0 mg/cm² and GPDC 4.0 mg/cm² cathodes were 19.7% and 9.8%, respectively. The porosity results are consistent to the (GPDC/cathode) mass-to-volume ratio. The increasing GPDC loading reduced the porosity of the cathode. These electrochemical performance results indicate that GPDC loading of 3.0 mg/cm² catalyst has shown the highest performance owing to the formation of a smooth and continuous layer on the LSCF backbone with reasonable porosity. Therefore, the GPDC 3.0 mg/cm² is further considered for the detailed understanding of ORR kinetics, and from now on the LSCF cathode with GPDC 3.0 mg/cm² will be termed as GPDC-coated LSCF for comparison with

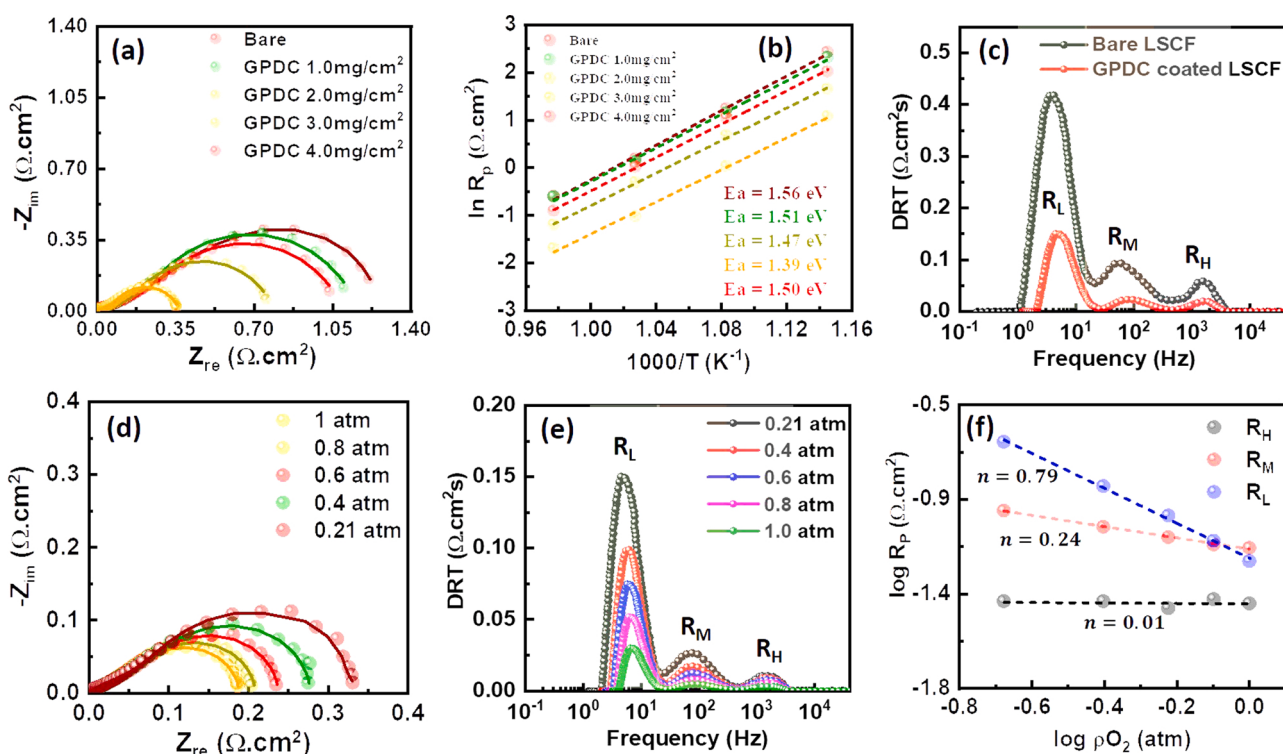


Fig. 4. Effect of GPDC on the ORR activity of LSCF (a) EIS spectra of LSCF with different loadings of GPDC catalysts at 700 °C in the air showing the lowest impedance at 3.0 mg/cm² GPDC loading. (b) Arrhenius plot of R_p and calculated activation energy values for oxide ions in the temperature range of 750–600 °C and as a function of different GPDC loadings. (c) DRT plot of bare LSCF and GPDC coated LSCF cathodes at 700 °C. (d) EIS spectra of GPDC coated LSCF at different $p\text{O}_2$ at 700 °C. (e) DRT spectra of GPDC coated LSCF for different $p\text{O}_2$ at 700 °C. (f) $\log p\text{O}_2$ dependence of R_p of GPDC coated LSCF electrode at 700 °C.

the bare LSCF electrode.

The ORR kinetics on the GPDC-infiltrated LSCF cathodes were studied by the EIS and results were analyzed using the distribution of relaxation time (DRT) method. Fig. 4(c) shows the DRT plot of the bare and GPDC-coated LSCF electrodes measured at 700 °C. The DRT plot for both bare and GPDC-coated LSCF electrodes showed three distinctive peaks in high frequency ($R_H \sim 10^4 - 10^3$ Hz), middle frequency (R_M , 100 – 500 Hz), and low frequency (R_L , 1 – 50 Hz) resistance region. To analyze the DRT behavior of the cells, EIS spectra of the GPDC-coated LSCF were measured as a function of oxygen partial pressure (ρO_2) through the adjustment of N_2 gas balance and the results are represented in Fig. 4(d). Fig. 4(d) shows that there R_p of the cathode has decreased gradually with the increase in the ρO_2 . For instance, the R_p value of GPDC coated LSCF electrode cell is $0.18 \Omega \cdot cm^2$ for ρO_2 of 1 atm and rises to $0.33 \Omega \cdot cm^2$ when ρO_2 drops to 0.21 atm (the air environment) which is ascribed to the enhanced oxygen concentration on the electrode surface. Fig. 4(e) shows the DRT plots obtained from EIS spectra as a function of ρO_2 . It can be observed that the peak area of R_H has not changed as a function of the ρO_2 , however, a small area variation is observed in the R_M region. On the other hand, there is a noticeable change in the R_L area peaks depicting that the processes taking place in the high-frequency region are independent of ρO_2 . On contrary, both R_M and R_L peak areas decreased much with the increase in the ρO_2 , demonstrating that the processes that occur in the middle and low-frequency range are dependent on the concentration of oxygen.

It is known that the ORR at the oxygen electrode is divided into several elementary steps and the rate-determining step can get from the n value of the following relationship between R_p of ORR and ρO_2 [65, 66]:

$$R_p = R_o \rho O_2^{-n} \quad (3)$$

Where R_o is a proportionality constant, and n is the order of a reaction. Herein, different values of n represent the different sub-processes of the ORR [67–69]. The R_H , R_M , and R_L resistances values were measured to calculate the n in Eq. (3). For this purpose, EIS spectra as a function of different ρO_2 were quantitatively analyzed by fitting to an equivalent circuit model (shown in Fig. S6, Supplementary Data). The equivalent circuit consists of three parallel R-CPE (R_H -CPE_H, R_M -CPE_M, and R_L -CPE_L) elements in series with an inductor (L). The added constant phase elements, CPE_H, CPE_M, and CPE_L, take part as a capacitive electrical response during the impedance analysis [59]. In the fitting of the EIS spectra, the individual real resistance (R_H , R_M , R_L) and constant phase elements CPE (CPE_H, CPE_M, and CPE_L) values were determined and shown in Table S1 (Supplementary Data). Fig. 4(f) shows the Arrhenius plots of log (ρO_2) versus log (R_p) with respect to R_H , R_M , and R_L variation. According to Fig. 4(f), the calculated n value from Eq. (3) for R_H , is 0.01 (close to zero), showing that the process at high frequency is related to the charge transfer process at the electrolyte/cathode interface [69–71]. The R_M showed the n value of 0.24 (close to 0.25) which is attributed to the surface diffusion of oxide ions [17, 67, 72]. On the other hand, the process for R_L ($n = 0.79$, close to 0.75) is closely related to the adsorption and dissociation of oxygen on the electrode surface [70, 73].

Based on the identified processes, it can be concluded that the coating of the GPDC catalyst significantly reduces the resistances in the entire frequency range (Fig. 3(c)) by enhancing the kinetics of the aforementioned processes occur in different frequency regions indicating the enormous improvement in the ORR kinetics by tailoring the surface of the LSCF electrode with highly conductive and robust GPDC coating. In general, sluggish kinetics of surface exchange of oxygen on LSCF governs the overall electrochemical performance, and Fig. 4 demonstrated that the infiltration of the GPDC catalyst remarkably accelerates the ORR kinetics on state-of-the-art LSCF air electrode.

3.4. Enhanced stability of GPDC-coated LSCF cathode under Cr atmosphere

To check the stability of GPDC-coated LSCF cathode in comparison to bare LSCF, we performed the durability test on symmetric cells in different atmospheres including dry air without Cr source, dry air with Cr source, and humidified (3 vol% H₂O) air with Cr source. Fig. S7(a) and (b) (Supplementary Data) exhibit the Nyquist plots of bare and GPDC-coated LSCF electrodes, respectively, measured at 700 °C in just dry air and Cr-containing dry and humidified atmospheres. The results showed that both bare and GPDC-coated LSCF cathodes showed relatively more R_p in humidified air and Cr-containing atmospheres. Therefore, we considered this stringent atmosphere to further study the stability of the bare and infiltrated electrodes for a prolonged time under these severe operating conditions. Fig. 5 represents a summary of the stability test in the form of impedance responses, polarization curves, and surface-enhanced Raman spectroscopy (SERS). Conforming to Fig. 5 (a), the ORR activity of bare LSCF dramatically deteriorated in the presence of humidified air and a Cr-containing atmosphere. For instance, the R_p is significantly raised from 1.51 to $2.01 \Omega \cdot cm^2$ after being polarized for 100 h under an applied current density of 0.2 mA/cm^2 (Fig. 5a), thereby, showing an increment of $0.5 \Omega \cdot cm^2$. In contrast, the GPDC-coated LSCF sample showed a pronounced tolerance against the humidified Cr-containing atmosphere with an R_p increase from 0.37 to $0.39 \Omega \cdot cm^2$ after 100 h of testing, thus, a minute increase of $0.02 \Omega \cdot cm^2$ (Fig. 5b). To elucidate the effect of Cr on each ORR step, we fitted the EIS spectra from Fig. 5(a) and (b) according to the equivalent circuit model shown in Fig. S6 (Supplementary Data). The results of equivalent fitting for both bare and GPDC-coated LSCF electrode cells are shown in Fig. 5(c) and (d), respectively. The bare LSCF electrodes cell revealed a significant increase in all resistances including R_H , R_M , and R_L suggesting that the kinetics of ORR associated with these resistances become sluggish with time when tested in a harsh Cr-containing atmosphere. However, it can be noticed from Fig. 5(c) that both R_M and R_L have contributed more to polarization losses with a total increment of 0.19 and $0.18 \Omega \cdot cm^2$, respectively, from the initial value. On the other hand, R_H has shown a very small rise of $0.05 \Omega \cdot cm^2$ from the initial value after the 100 h testing. Incoherent to this, the measured cathodic overpotential (η_c) at 0.2 A/cm^2 of GPDC-coated LSCF cathode, shown in Fig. S8 (Supplementary Data), tends to remain more stable with time than that of bare LSCF. The increase in the η_c results is consistent with the EIS represented in Fig. 5(a) and (b). This indicates that the Cr-containing atmospheres significantly reduce the kinetics of the processes occurring in the middle and low-frequency range i.e., surface chemical exchange of oxide ions. The slight polarization loss of $0.05 \Omega \cdot cm^2$ in R_H could be related to the small amount of formation of secondary phases on the cathode/electrolyte interface [74]. The GPDC-coated porous LSCF electrode cell showed a stable trend in all resistances i.e., R_H , R_M , and R_L , as shown in Fig. 5(d) indicating that the application of GPDC coating to LSCF notably stabilizes the oxygen surface exchange reaction even in the stringent Cr-containing humid atmospheres.

To explain the possible reasons for the degradation of bare LSCF and good stability of GPDC-coated LSCF, SERS was performed. SERS is a prevailing characterization technique to detect the trace number of secondary phases which has low-intensity signals [75, 76]. In typical SOFC cathodes, such secondary phases have low concentrations and are ceramic, and possess weak Raman modes. SERS is a viable solution to cope with this problem in which the signals mainly come from the surface of the materials under consideration allowing to detection of the secondary phases even in trace amounts present on the surface of the electrode with increased intensities [77, 78]. In this study, we performed SERS on reference dense bare and GPDC-coated LSCF pellets after testing them under identical SOFC conditions (i.e., humidified Cr atmosphere, at 700 °C and 0.2 A/cm^2) for different periods. The detailed procedure of performing SERS on the dense LSCF and GPDC-coated LSCF

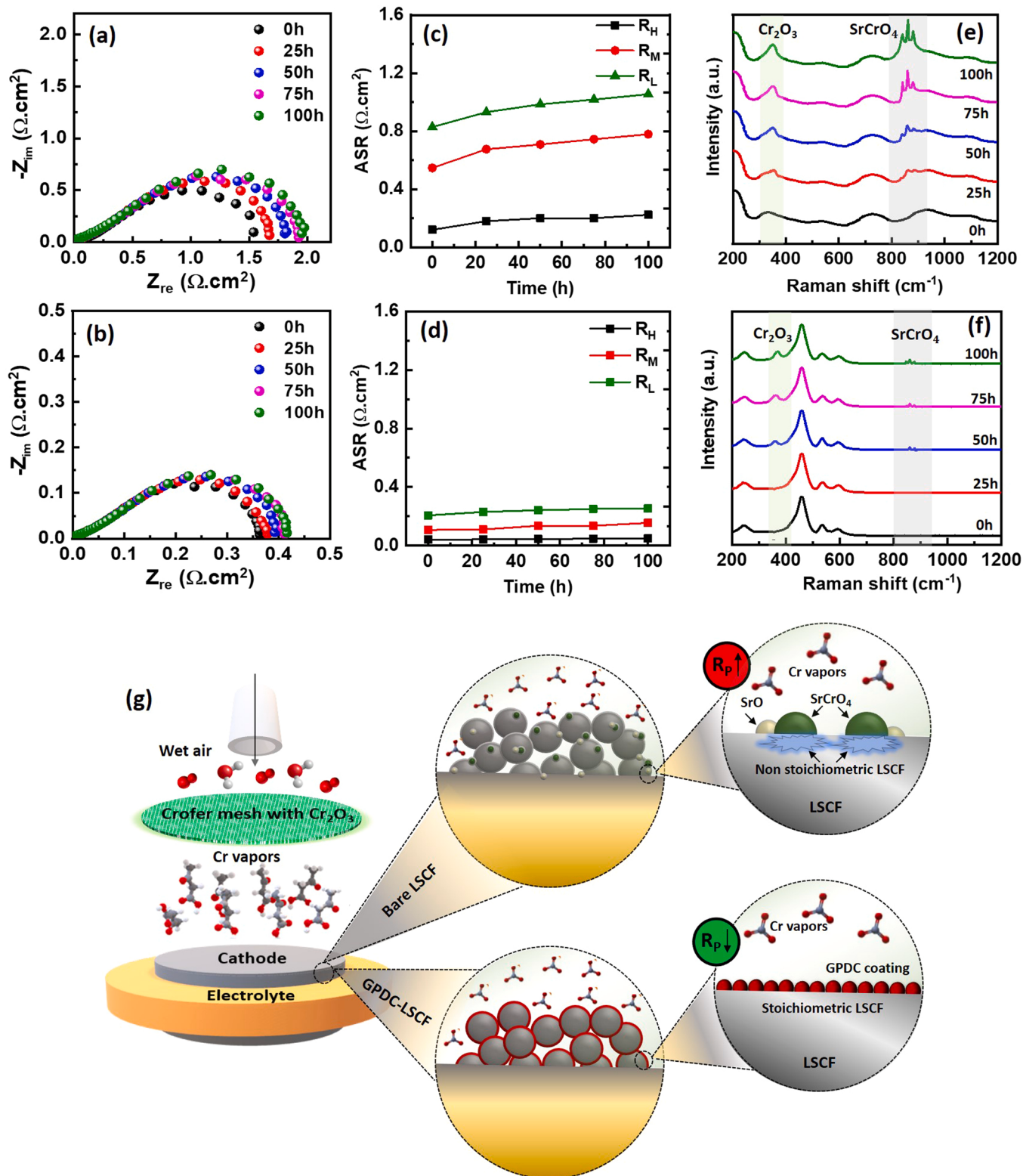


Fig. 5. Nyquist plot measured at 700 °C under OCV conditions as a function of time in a Cr-containing and humid atmosphere for the cells with (a) bare LSCF and (b) GPDC coated LSCF, resistance values as a function of operating time determined by equivalent impedance circuit model for the cells with (c) bare LSCF and (d) GPDC coated LSCF, SERS spectra at different operating times in Cr-containing and humid atmospheres for (e) bare LSCF and (f) GPDC coated LSCF (g) Schematic description of surface chemistry of bare LSCF and GPDC coated LSCF cathodes during long-term testing in Cr-containing and humid atmospheres.

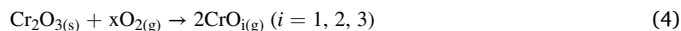
pellets is schematically shown in Fig. S9(a) (Supplementary Data).

Fig. 5(e) presents the SERS results of pristine LSCF (before the test) exhibiting different peaks at 200, 320, 540, 725, 950, and 1130 cm^{-1} belonging to the R3c space group corresponding to the peaks of the

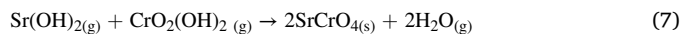
perovskite phase [79]. However, multiple peaks between $\sim 840 \text{ cm}^{-1}$ and 860 cm^{-1} are observed in addition to the satellite peak at $\sim 360 \text{ cm}^{-1}$ when the LSCF electrode is tested in Cr containing humid atmosphere. The peaks at 360 cm^{-1} and between 840 and 860 cm^{-1}

suggest the formation of the Cr_2O_3 and SrCrO_4 , respectively [34,79]. It is also observed from Fig. 5(e) that the peak intensities of Cr_2O_3 and SrCrO_4 are increased with time (0 – 100 h) when the bare LSCF is exposed to the humidified Cr atmosphere indicating the rise in the degree of Cr poisoning of the bare LSCF. On the contrary, the GPDC-coated LSCF exhibits the significantly weak SERS modes of Cr_2O_3 and SrCrO_4 (Fig. 5(f)) at all periods, thus, showing the mitigating effects of Cr poisoning. Moreover, these results of the Cr poisoning are consistent with the increase in the polarization resistance of the bare and GPDC-coated LSCF electrode cells.

According to the SERS results, it is found that Cr is mainly present as Cr_2O_3 and SrCrO_4 . The Cr_2O_3 is evaporated at higher temperatures and generates gaseous species (e.g., CrO_3 and Cr(OH)_3) via the following reactions [74,80,81]:



These gaseous Cr species diffuse into the pores of the LSCF cathode and are ultimately deposited on the cathode and cathode/electrolyte interface in the form of Cr_2O_3 , which acts as a barrier for ORR. Additionally, SrCrO_4 is also formed when Cr species react with the segregated SrO or Sr(OH)_2 on the surface of bare LSCF in humid air according to the following reaction [82,83]:



The abrupt increase in R_M and R_L in bare LSCF (Fig. 5c) is attributed to the formation of inert phases of Cr_2O_3 and SrCrO_4 on the bare LSCF surface which retards the surface exchange reaction of oxygen, thereby, leading to a fast increase in the polarization resistance of the cell. Nevertheless, the GPDC-coated LSCF showed weak relative intensities of Cr_2O_3 as well as SrCrO_4 peaks which justifies the enhanced stability in R_M and R_L . To visualize the intensity difference between Cr_2O_3 and SrCrO_4 in both bare and GPDC-coated electrodes, the intensity values of SERS spectra of pristine samples were subtracted (i.e., differential analysis with respect to pristine conditions) from the Cr-poisoned samples as a function of time and results are shown in Fig. S9 (b) and (c), respectively (Supplementary Data). It can be seen from Fig. S9 (b) (Supplementary Data) that the peak intensity of SrCrO_4 is more prominent than that of Cr_2O_3 suggesting that SrCrO_4 formation contributes more to the degradation of the LSCF cathode. It is worth mentioning that the Cr_2O_3 peak is still observed in GPDC-coated LSCF but the intensity of this peak is significantly low compared to that of bare LSCF cells. However, the GPDC-coated LSCF significantly reduces the formation of SrCrO_4 (Fig. S9 (c), Supplementary Data) than that of bare LSCF reflecting that the coating of GPDC catalyst on the LSCF surface prevents the formation of segregated SrO , which is a vital component in the formation of SrCrO_4 . To explain this, Le et al. [84] found that the ionic radii mismatch between cations in perovskite generates negatively charged defects (D_A^-) and positive surface oxygen vacancies (V_O^+). The electrostatic interaction between D_A^- and V_O^+ drives the cations toward the surface where they form insulating oxides. Mebane et al. [85] also confirmed that cation segregation in perovskites is more favored at V_O^+ for the free surface. Ding et al. [86] explained possible ways through first-principles calculations to suppress the Sr segregation in LSCF cathodes. One of them is to apply the compressive strain on the LSCF either by incorporating a larger dopant or by coating the surface of the LSCF. Therefore, in this study, the application of GPDC coating to the surface of LSCF reduces the V_O^+ concentration at the surface of the LSCF thereby suppressing the surface Sr segregation, and hence negligible SrCrO_4 is formed in GPDC-coated LSCF. This explains how the surface coating of LSCF with GPDC catalysts outstandingly enhances the tolerance of LSCF against harsh Cr atmospheres. The proposed degradation mechanism of bare LSCF and mitigation strategy by GPDC coating LSCF

under Cr atmosphere is schematically shown in Fig. 5(g), depicting the promotional effect of suppressed Sr segregation by GPDC.

3.5. Electrochemical performance of anode-supported SOFC with GPDC-coated LSCF cathode

The increased ORR activity and durability of the GPDC-coated LSCF electrode were further tested in a single anode-supported SOFC in the temperature range of 650–750 °C by supplying 3 vol% humidified H_2 and ambient air to the anode and cathode, respectively. A cross-section of anode-supported SOFC and SEM images of LSCF and GPDC-coated LSCF cathode are shown in Fig. S10 (Supplementary Data). Fig. 6(a) compares the I-V curves of bare LSCF and GPDC-coated LSCF cathode cells at 700 °C. The measured OCV for both cells is close to ~1.102 V, indicating no gas leakage through the electrolyte and sealant. The bare LSCF cathode cell has shown a maximum power density (P_{\max}) of 0.76 W/cm², whereas the cell with GPDC coated LSCF cathode exhibited a P_{\max} of 1.49 W/cm² which is almost double of that bare LSCF cell. Fig. 6(b) and (c) represent the Nyquist and Bode plots, respectively for bare and GPDC-coated LSCF cathode cells. Fig. 6(b) shows the high ohmic resistance (R_O , 0.32 Ω cm²) and R_p (0.63 Ω cm²) compared to that of GPDC coated LSCF ((R_O , 0.25 Ω cm² and R_p , 0.28 Ω cm²). The decrease in impedance by coating the LSCF with GPDC is associated with the reduction in both high (10^4 – 10^3 Hz) and low frequency (1–100 Hz) arcs as shown in Fig. 6(c). The reduction in the high and low-frequency regions in GPDC-coated LSCF is attributed to the improvement in the charge transfer resistance and ORR activity, respectively [87]. The GPDC-coated LSCF also showed enhanced electrochemical performance compared to the bare LSCF at other temperatures (Figs. S11 and S12, Supplementary Data).

To check the stability of GPDC-coated LSCF in full SOFCs, a long-term test of ~500 h was conducted at an applied current density of 0.5 A/cm² at 700 °C by exposing the cathode in Cr and humid air (3 vol % H_2O) atmospheres and results are displayed in Fig. 6(d). Consistent with the stability results of half cells, the GPDC coating on LSCF remarkably improves the degradation rate of LSCF from 0.29% to 0.006% h⁻¹. EIS spectra were measured for both cathodes after their testing in Cr atmospheres which shows the stable R_p of SOFC with GPDC-coated LSCF cathode as shown in Fig. 6(e). SEM coupled with an EDS line scan was performed on the tested electrodes which shows the significant deposition of Cr species on bare LSCF surface as well as at the cathode/electrolyte interface (Fig. S13 (a), Supplementary Data). On contrary, GPDC-coated LSCF showed negligible co-presence of Sr and Cr on the surface and interfaces explaining the better stability at 700 °C (Fig. S13 (b), Supplementary Data). It can be noticed from Fig. S13 (a) (Supplementary Data) that for the bare LSCF electrode in contact with the Cr-containing alloy, the features of the SrCrO_4 peak are more prominent on/near the LSCF-GDC interface, suggesting preferential deposition of SrCrO_4 in these areas, due to most likely the more SrO segregation on the grain surface caused by the higher local oxygen partial pressure during the long-term testing.

Moreover, it is necessary to compare the results of this study with the literature. For this purpose, a promotion factor, defined by the ratio of obtained P_{\max} of the catalyst-coated electrode to that of the bare electrode (i.e., $P_{\max, \text{coated}}/P_{\max, \text{bare}}$), is calculated and compared with the results of other catalyst-coated LSCF electrodes, as presented in Fig. 6(f). The calculated promotion factor for GPDC-coated LSCF is ~2 which is higher than other catalysts-coated LSCF cathodes indicating the performance boost of GPDC catalyst coating over other catalyst coatings for LSCF electrodes. In Table S3 (Supplementary Data), the output powers of GPDC-coated LSCF SOFCs are compared with those of other catalyst-coated LSCF SOFCs showing that GPDC coating gives a higher MPD than other catalyst coatings for LSCF cathode. The degradation rates of different catalyst-coated LSCF electrodes in humid air and Cr atmospheres with operating conditions are shown in Table 1.

According to our study, the degradation rate for bare LSCF at 700 °C

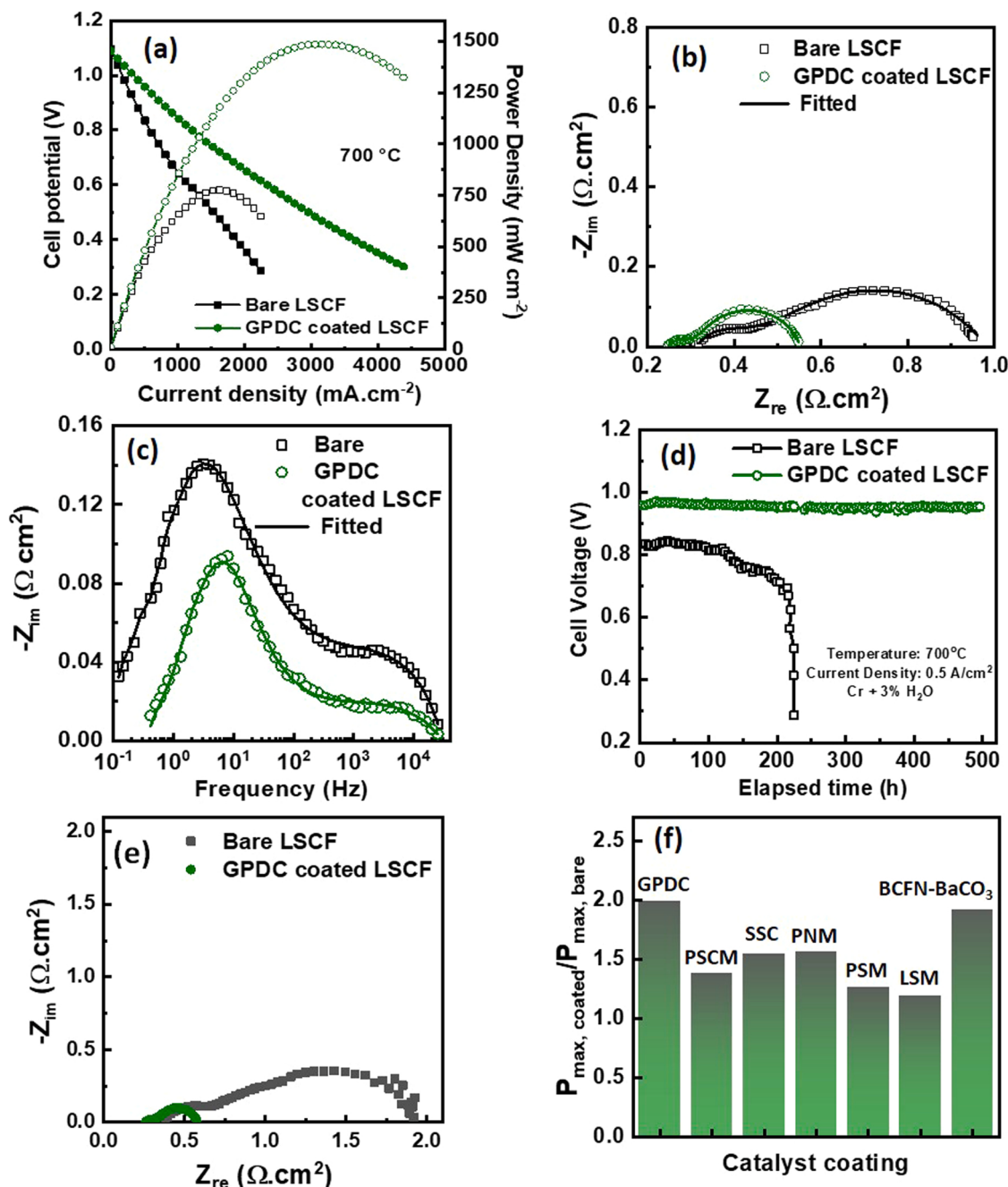


Fig. 6. Electrochemical performance comparison between bare and GPDC coated LSCF cathode single anode-supported SOFC, measured at 700 °C (a) I-V-P curves, (b) Nyquist plot, (c) Bode plot, (d) stability test under a galvanostatic load of 0.5 A/cm² in Cr-3 vol% humidified atmosphere, and (e) Nyquist plot of SOFC with bare and GPDC coated LSCF cathode cell measured before and after long-term testing at OCV conditions. (f) Measured P_{max, coated}/P_{max, bare} ratio of different catalysts coatings for LSCF electrode at 750 °C in ambient air: GPDC (this study), PrSrCoMnO_{6-d} (PSCM) [33], Sm_{0.5}Sr_{0.5}CoO₃ (SSC) [88], PrNi_{0.5}Mn_{0.5}O₃ (PNM) [89], Pr_{0.75}Sr_{0.2}MnO_{3-d} (PSM) [33], La_{0.85}Sr_{0.15}MnO₃ (LSM) [33], and BaCo_{1-x-y}Fe_xNb_yO_{3-d} (BCFN)-BaCO₃ [90].

is 0.29% h⁻¹, which is comparable to similar studies under identical conditions. The degradation rate for GPDC-coated LSCF electrodes is 0.006% h⁻¹, which is almost ten times lower than those reported with other catalyst coatings on LSCF electrodes (Table 1), demonstrating that GPDC coating achieves magnificent stability under Cr atmospheres with minimum degradation rates for LSCF electrodes so far. As a highly active and Cr-tolerant cathode for SOFCs, the GPDC-coated LSCF shows high chromium tolerance under accelerated Cr poisoning conditions, thus, suggesting that GPDC-coated LSCF cathode is a promising material with enhanced performance and durability.

4. Conclusion

In this study, we have synthesized a novel Gd and Pr multi-doped ceria (GPDC, Gd_{0.2-x}Pr_xCe_{0.8}O_{2-δ}; x = 0, 0.02, 0.04, 0.06, 0.08, 0.1, and 0.15) by sol-gel process and showed that GPDC with nominal composition of Gd_{0.1}Pr_{0.1}Ce_{0.8}O_{2-δ} exhibits 42% higher conductivity compared to GDC. Based on this, the optimized GPDC catalyst is incorporated into the state-of-the-art LSCF electrode by the wet infiltration method with different loadings. The results demonstrated that GPDC loading of 3 mg/cm² forms a conformal coating on the LSCF electrode surface which led to a ~71% reduction in the R_p of the LSCF

Table 1

Degradation rates of various SOFCs operating in Cr and humidified air atmospheres compared with different catalyst-coated LSCF electrodes described in the literature.

Coating material on LSCF electrode	Cell type	Conditions	Degradation rate (% per hour)	Ref.
GPDC	Ni-YSZ anode-supported cell	700 °C, 0.5 Acm ⁻²	Coated: 0.006, Bare: 0.29	This study
BCFN-BaCO ₃	Ni-YSZ anode-supported cell	650 °C, 0.25 Acm ⁻²	Coated: 0.05, Bare: 0.13	[90]
PNM	Ni-YSZ anode-supported cell	750 °C, 0.7 V	Coated: 0.04, Bare: 0.4	[89]
BaCoO _{3-x} (BCO) ^a	Ni-YSZ anode-supported cell	700 °C, 0.7 V	Coated: 0.056, Bare: 0.31	[91]
BaO ^b	LSCF/GDC/Pt half cells ^b	800 °C, 0.2 Acm ⁻²	Coated: 0.18, Bare: 16	[92]
GDC	LSCF/GDC/Pt half cells ^b	800 °C, 0.2 Acm ⁻²	Coated: 0.21, Bare: 16	[36]

^a Nanoparticles.

^b Degradation rates of half-cells were calculated based on the change in the RP of half-cells before and after testing.

cathode compared to the bare LSCF cathode cell. This significant reduction in R_p is attributed to the substantial improvement in the oxygen surface exchange reaction of LSCF. In addition, the GPDC-coated LSCF electrode cell showed better stability in R_p of symmetric cells for 100 h at 700 °C in stringent Cr-containing atmospheres which is attributed to the negligible formation in SrCrO₄ as indicated by the SERS results. The SOFC with GPDC coated LSCF cathode showed MPD of 1.48 W/cm² at 700 °C which is almost double compared to the cell with bare LSCF cathode as well as remarkable durability during 500 h operation in harsh Cr and humid air atmospheres with the degradation rates of 0.001% h⁻¹ at 700 °C. The strategy presented in this study helps commercialize SOFC technology with enhanced efficiency and reliability and has the potential to be adopted in other energy conversion systems such as solid oxide electrolysis and dye-sensitized solar cells.

CRediT authorship contribution statement

Hafiz Ahmad Ishfaq: Conceptualization, Methodology, Writing – original draft, Methodology, Validation, Resources. **Muhammad Zubair Khan:** Conceptualization, Investigation, Methodology, Formal analysis, Validation, Writing – original draft, Writing – review & editing, Resources, Supervision. **Yogita Manikrao Shirke:** Formal analysis, Writing – review & editing. **Sanaullah Qamar:** Investigation, Writing – original draft. **Amjad Hussain:** Methodology, Writing – review & editing. **Muhammad Taqi Mehran:** Methodology, Writing – review & editing, Resources. **Rak-Hyun Song:** Methodology, Visualization, Investigation. **Mohsin Saleem:** Methodology, Writing – review & editing.

Declaration of Competing Interest

The authors declare that they have no known competing financial interests or personal relationships that could have appeared to influence the work reported in this paper.

Data availability

Data will be made available on request.

Acknowledgments

The authors acknowledge the technical resources and lab facilities from the Pak-Austria Fachhochschule: Institute of Applied Sciences and Technology, Haripur, Pakistan, National University of Sciences and

Technology (NUST), Islamabad, Pakistan, and National Institute of Chemistry, Ljubljana, Slovenia.

Appendix A. Supplementary material

Supplementary data associated with this article can be found in the online version at doi:10.1016/j.apcatb.2022.122178.

References

- H. Moon, S.D. Kim, S.H. Hyun, H.S. Kim, Development of IT-SOFC unit cells with anode-supported thin electrolytes via tape casting and co-firing, Int. J. Hydrog. Energy 33 (2008) 1758–1768, <https://doi.org/10.1016/j.ijhydene.2007.12.062>.
- M.Z. Khan, M.T. Mehran, R.H. Song, J.W. Lee, S.B. Lee, T.H. Lim, S.J. Park, Effect of GDC interlayer thickness on durability of solid oxide fuel cell cathode, Ceram. Int. 42 (2015) 6978–6984, <https://doi.org/10.1016/j.ceramint.2016.01.085>.
- M.Z. Khan, R.-H. Song, A. Hussain, S.-B. Lee, T.-H. Lim, J.-E. Hong, Effect of applied current density on the degradation behavior of anode-supported flat-tubular solid oxide fuel cells, J. Eur. Ceram. Soc. 40 (2020) 1407–1417, <https://doi.org/10.1016/j.jeurceramsoc.2019.11.017>.
- J. Peng, J. Huang, X. long Wu, Y. wu Xu, H. Chen, X. Li, Solid oxide fuel cell (SOFC) performance evaluation, fault diagnosis and health control: a review, J. Power Sources 505 (2021), <https://doi.org/10.1016/j.jpowsour.2021.230058>.
- M. Liu, M.E. Lynch, K. Blinn, F.M. Alamgir, Y. Choi, Rational SOFC material design: new advances and tools, Mater. Today 14 (2011), [https://doi.org/10.1016/S1369-7021\(11\)70279-6](https://doi.org/10.1016/S1369-7021(11)70279-6).
- E.D. Wachsman, K.T. Lee, Lowering the temperature of solid oxide fuel cells, Science 334 (2011) (1979), <https://doi.org/10.1126/science.1204090>.
- T. Raza, J. Yang, R. Wang, C. Xia, R. Raza, B. Zhu, S. Yun, Recent advance in physical description and material development for single component SOFC: a mini-review, Chem. Eng. J. 444 (2022), 136533, <https://doi.org/10.1016/J.CEJ.2022.136533>.
- L. Li, Z. Kong, B. Yao, H. Yang, Z. Gao, L. Xu, F. Dong, M. Ni, Z. Lin, An efficient and durable perovskite electrocatalyst for oxygen reduction in solid oxide fuel cells, Chem. Eng. J. 396 (2020), <https://doi.org/10.1016/j.cej.2020.125237>.
- A. Ndubuisi, S. Abouali, K. Singh, V. Thangadurai, Recent advances, practical challenges, and perspectives of intermediate temperature solid oxide fuel cell cathodes, J. Mater. Chem. A Mater. 10 (2022), <https://doi.org/10.1039/dta08475e>.
- M.Z. Khan, R.H. Song, S.B. Lee, T.H. Lim, Lifetime prediction of anode-supported solid oxide fuel cell on the basis of individual components degradation, ECS Trans. (2019), <https://doi.org/10.1149/09101.0621ecst>.
- M. Singh, D. Zappa, E. Comini, Solid oxide fuel cell: decade of progress, future perspectives and challenges, Int. J. Hydrog. Energy 46 (2021), <https://doi.org/10.1016/j.ijhydene.2021.06.020>.
- M.Z. Khan, R.-H. Song, M.T. Mehran, S.-B. Lee, T.-H. Lim, Controlling cation migration and inter-diffusion across cathode/interlayer/electrolyte interfaces of solid oxide fuel cells: a review, Ceram. Int. 47 (2021) 5839–5869, <https://doi.org/10.1016/j.ceramint.2020.11.002>.
- D.W. Joh, A. Cha, J.H. Park, K.J. Kim, K.T. Bae, D. Kim, Y.K. Choi, H. An, J.S. Shin, K.J. Yoon, K.T. Lee, In situ synthesized La_{0.6}Sr_{0.4}Co_{0.2}Fe_{0.8}O_{3-δ}-Gd_{0.1}Ce_{0.9}O_{1.95} nanocomposite cathodes via a modified sol-gel process for intermediate temperature solid oxide fuel cells, ACS Appl. Nano Mater. 1 (2018), <https://doi.org/10.1021/acsm.nano.8b00566>.
- S.J. Skinner, J.A. Kilner, Oxygen ion conductors, Mater. Today 6 (2003) 30–37, [https://doi.org/10.1016/S1369-7021\(03\)00322-8](https://doi.org/10.1016/S1369-7021(03)00322-8).
- S. Il Lee, J. Kim, J.W. Son, J.H. Lee, B.K. Kim, H.J. Je, H.W. Lee, H. Song, K.J. Yoon, High performance air electrode for solid oxide regenerative fuel cells fabricated by infiltration of nano-catalysts, J. Power Sources 250 (2014) 15–20, <https://doi.org/10.1016/J.JPOWSOUR.2013.10.123>.
- Q. Zhang, Y. Hou, L. Chen, L. Wang, K. Chou, Enhancement of electrochemical performance for proton conductive solid oxide fuel cell by 30%GDC-LSCF cathode, Ceram. Int. 48 (2022) 17816–17827, <https://doi.org/10.1016/J.CERAMINT.2022.03.052>.
- J.H. Park, C.H. Jung, K.J. Kim, D. Kim, H.R. Shin, J.E. Hong, K.T. Lee, Enhancing bifunctional electrocatalytic activities of oxygen electrodes via incorporating highly conductive Sm₃₊and Nd₃₊+double-doped ceria for reversible solid oxide cells, ACS Appl. Mater. Interfaces 13 (2021), <https://doi.org/10.1021/acsm.0c17238>.
- M.E. Brito, H. Morishita, J. Yamada, H. Nishino, H. Uchida, Further improvement in performances of La_{0.6}Sr_{0.4}Co_{0.2}Fe_{0.8}O_{3-δ} - doped ceria composite oxygen electrodes with infiltrated doped ceria nanoparticles for reversible solid oxide cells, J. Power Sources 427 (2019) 293–298, <https://doi.org/10.1016/J.JPOWSOUR.2019.04.066>.
- M.Z. Khan, M.T. Mehran, R.-H. Song, J.-W. Lee, S.-B. Lee, T.-H. Lim, S.-J. Park, Effect of GDC interlayer thickness on durability of solid oxide fuel cell cathode, Ceram. Int. 42 (2016) 6978–6984, <https://doi.org/10.1016/j.ceramint.2016.01.085>.
- M.Z. Khan, R.-H. Song, S.-B. Lee, J.-W. Lee, T.-H. Lim, S.-J. Park, Effect of GDC interlayer on the degradation of solid oxide fuel cell cathode during accelerated current load cycling, Int. J. Hydrog. Energy 39 (2014) 20799–20805, <https://doi.org/10.1016/j.ijhydene.2014.07.022>.

[21] M.Z. Khan, M.T. Mehran, R.H. Song, S.B. Lee, T.H. Lim, Effects of applied current density and thermal cycling on the degradation of a solid oxide fuel cell cathode, *Int. J. Hydron. Energy* 43 (2018) 12346–12357, <https://doi.org/10.1016/j.ijhydene.2018.04.175>.

[22] D.W. Joh, J.H. Park, D. Kim, E.D. Wachsman, K.T. Lee, Functionally graded bismuth oxide/zirconia bilayer electrolytes for high-performance intermediate-temperature solid oxide fuel cells (IT-SOFCs), *ACS Appl. Mater. Interfaces* 9 (2017) 8443–8449, <https://doi.org/10.1021/acsami.6b16660>.

[23] S. Anirban, T. Paul, P.T. Das, T.K. Nath, A. Dutta, Microstructure and electrical relaxation studies of chemically derived Gd–Nd co-doped nanocrystalline ceria electrolytes, *Solid State Ion.* 270 (2015) 73–83, <https://doi.org/10.1016/J.SSI.2014.12.011>.

[24] S. Dikmen, Effect of co-doping with Sm³⁺, Bi³⁺, La³⁺, and Nd³⁺ on the electrochemical properties of hydrothermally prepared gadolinium-doped ceria ceramics, *J. Alloy. Compd.* 491 (2010) 106–112, <https://doi.org/10.1016/J.JALCOM.2009.11.006>.

[25] K.T. Lee, A.A. Lidie, H.S. Yoon, E.D. Wachsman, Rational design of lower-temperature solid oxide fuel cell cathodes via nanotailoring of co-assembled composite structures, *Angew. Chem. Int. Ed.* 53 (2014), <https://doi.org/10.1002/anie.201408210>.

[26] D.A. Andersson, S.I. Simak, N.V. Skorodumova, I.A. Abrikosov, B. Johansson, Optimization of ionic conductivity in doped ceria, *Proc. Natl. Acad. Sci. USA* 103 (2006), <https://doi.org/10.1073/pnas.0509537103>.

[27] S. Omar, E.D. Wachsman, J.C. Nino, Higher conductivity Sm³⁺ and Nd³⁺ co-doped ceria-based electrolyte materials, *Solid State Ion.* 178 (2008), <https://doi.org/10.1016/j.ssi.2007.12.069>.

[28] H.L. Tuller, S.R. Bishop, D. Chen, Y. Kuru, J.-J. Kim, T.S. Stefanik, Praseodymium doped ceria: Model mixed ionic electronic conductor with coupled electrical, optical, mechanical and chemical properties, *Solid State Ion.* 225 (2012) 194–197, <https://doi.org/10.1016/j.ssi.2012.02.029>.

[29] Y. Li, W. Zhang, Y. Zheng, J. Chen, B. Yu, Y. Chen, M. Liu, Controlling cation segregation in perovskite-based electrodes for high electro-catalytic activity and durability, *Chem. Soc. Rev.* 46 (2017) 6345–6378, <https://doi.org/10.1039/c7cs00120g>.

[30] J. Li, X. Zhou, C. Wu, L. Zhao, B. Dong, S. Wang, B. Chi, Self-stabilized hybrid cathode for solid oxide fuel cell: A-site deficient perovskite coating as solid solution for strontium diffusion, *Chem. Eng. J.* 438 (2022), 135446, <https://doi.org/10.1016/J.CEJ.2022.135446>.

[31] T.H. Kim, M.Z. Khan, R.H. Song, S.B. Lee, T.H. Lim, J.E. Hong, Development of oxide dispersed ferritic steel as a solid oxide fuel cell interconnect, *ECS Trans.* (2019), <https://doi.org/10.1149/09101.2307ecst>.

[32] T. Horita, Chromium poisoning for prolonged lifetime of electrodes in solid oxide fuel cells - Review, *Ceram. Int.* 47 (2021) 7293–7306, <https://doi.org/10.1016/J.CERAMINT.2020.11.082>.

[33] D. Ding, M. Liu, Z. Liu, X. Li, K. Blinn, X. Zhu, M. Liu, Efficient electro-catalysts for enhancing surface activity and stability of SOFC cathodes, *Adv. Energy Mater.* 3 (2013), <https://doi.org/10.1002/aenm.201200984>.

[34] Y. Chen, Y.M. Choi, S. Yoo, Y. Ding, R. Yan, K. Pei, C. Qu, L. Zhang, I. Chang, B. Zhao, Y. Zhang, H. Chen, Y. Chen, C. Yang, B. deGlee, R. Murphy, J. Liu, M. Liu, A highly efficient multi-phase catalyst dramatically enhances the rate of oxygen reduction, *Joule* 2 (2018) 938–949, <https://doi.org/10.1016/J.JOULE.2018.02.008>.

[35] L. Zhao, Y. Cui, L. Gui, G. Li, B. He, A comparison study of chromium deposition and poisoning on La_{0.8}Sr_{0.2}Ga_{0.8}Mg_{0.2}O_{3-δ} and Gd_{0.1}Ce_{0.9}O_{2-δ} electrolytes of solid oxide fuel cells, *J. Alloy. Compd.* 688 (2016), <https://doi.org/10.1016/j.jallcom.2016.07.070>.

[36] L. Zhao, S. Amarasinghe, S.P. Jiang, Enhanced chromium tolerance of La_{0.6}Sr_{0.4}Co_{0.2}Fe_{0.8}O_{3-δ} electrode of solid oxide fuel cells by Gd_{0.1}Ce_{0.9}O_{1.95} impregnation, *Electrochim. Commun.* 37 (2013), <https://doi.org/10.1016/j.elecom.2013.10.019>.

[37] D. Ding, X. Li, S.Y. Lai, K. Gerdes, M. Liu, Enhancing SOFC cathode performance by surface modification through infiltration, *Energy Environ. Sci.* 7 (2014), <https://doi.org/10.1039/c3ee42926a>.

[38] H.A. Ishfaq, M.Z. Khan, M.T. Mehran, R. Raza, W.H. Tanveer, S. Bibi, A. Hussain, H.A. Muhammad, R.H. Song, Boosting performance of the solid oxide fuel cell by facile nano-tailoring of La_{0.6}Sr_{0.4}Co_{0.3}-δ cathode, *Int. J. Hydron. Energy* (2021), <https://doi.org/10.1016/J.IJHYDENE.2021.11.109>.

[39] S.U. Rehman, A. Shaur, H.S. Kim, D.W. Joh, R.H. Song, T.H. Lim, J.E. Hong, S. J. Park, S.B. Lee, Effect of transition metal doping on the sintering and electrochemical properties of GDC buffer layer in SOFCs, *Int. J. Appl. Ceram. Technol.* 18 (2021), <https://doi.org/10.1111/ijac.13650>.

[40] Y. Long, J. Duval, M. Li, C. Gu, Z. Liu, S.P. Ringer, Electrical conductivity studies on individual conjugated polymer nanowires: two-probe and four-probe results, *Nanoscale Res. Lett.* 5 (2010) 237, <https://doi.org/10.1007/s11671-009-9471-y>.

[41] W. ZAJAC, Electrical conductivity of doubly doped ceria, *Solid State Ion.* 179 (2008) 154–158, <https://doi.org/10.1016/j.ssi.2007.12.047>.

[42] A. Shaur, S.U. Rehman, H.S. Kim, R.H. Song, T.H. Lim, J.E. Hong, S.J. Park, S. B. Lee, Hybrid electrochemical deposition route for the facile nanofabrication of a Cr-poisoning-tolerant La(Ni,Fe)O₃-δ cathode for solid oxide fuel cells, *ACS Appl. Mater. Interfaces* 12 (2020), <https://doi.org/10.1021/acsami.9b17807>.

[43] M. Irshad, K. Siraj, R. Raza, F. Javed, M. Ahsan, I. Shakir, M.S. Rafique, High performance of SDC and GDC core shell type composite electrolytes using methane as a fuel for low temperature SOFC, *AIP Adv.* 6 (2016), 025202, <https://doi.org/10.1063/1.4941676>.

[44] R.D. Shannon, Revised effective ionic radii and systematic studies of interatomic distances in halides and chalcogenides, *Acta Crystallogr. Sect. A* 32 (1976), <https://doi.org/10.1107/S0567739476001551>.

[45] J.H. Park, K.J. Kim, C.H. Jung, W. Jeong, H.R. Shin, J. -E. Hong, K.T. Lee, Boosting the performance of solid oxide electrolysis cells via incorporation of Gd³⁺ and Nd³⁺ double-doped Ceria, *Fuel Cells* 20 (2020) 712–717, <https://doi.org/10.1002/fuce.201900248>.

[46] L. Vegard, H. Dale, VIII. Untersuchungen über Mischkristalle und Legierungen, *Z. Kristallogr. Cryst. Mater.* 67 (1928), <https://doi.org/10.1524/zkri.1928.67.1.148>.

[47] S. Grieshammer, The effect of defect interactions on the reduction of doped ceria, *Phys. Chem. Chem. Phys.* 23 (2021), <https://doi.org/10.1039/d1cp00925g>.

[48] J. Koettgen, S. Grieshammer, P. Hein, B.O.H. Grope, M. Nakayama, M. Martin, Understanding the ionic conductivity maximum in doped ceria: trapping and blocking, *Phys. Chem. Chem. Phys.* 20 (2018), <https://doi.org/10.1039/c7cp0853d>.

[49] J. Faber, C. Geoffroy, A. Roux, A. Sylvestre, P. Abéard, A Systematic investigation of the dc electrical conductivity of rare-earth doped ceria, *Appl. Phys. A Solids Surf.* 49 (1989), <https://doi.org/10.1007/BF00616848>.

[50] G. Bin Jung, T.J. Huang, C.L. Chang, Effect of temperature and dopant concentration on the conductivity of samaria-doped ceria electrolyte, *J. Solid State Electrochem.* 6 (2002), <https://doi.org/10.1007/s100080100238>.

[51] A.D. Liyanage, S.D. Perera, K. Tan, Y. Chabal, K.J. Balkus, Synthesis, characterization, and photocatalytic activity of Y-doped CeO₂ nanorods, *ACS Catal.* 10 (2020) 577–584, <https://doi.org/10.1021/cs400889y>.

[52] M. Romeo, K. Bak, J. el Fallah, F. le Normand, L. Hilaire, XPS Study of the reduction of cerium dioxide, *Surf. Interface Anal.* 20 (1993) 508–512, <https://doi.org/10.1002/sia.740200604>.

[53] C. Sun, G. He, L. Gao, S. Song, R. Li, Q. Zhen, Absorption behavior of lattice oxygen in Ce_{0.8}Y_{0.2}O₂₋ at intermediate temperature, *J. Rare Earths* 36 (2018) 630–634, <https://doi.org/10.1016/j.jre.2018.01.007>.

[54] J. Liu, C. Zhu, D. Zhu, X. Jia, Y. Zhang, J. Yu, X. Li, M. Yang, High performance low-temperature solid oxide fuel cells based on nanostructured ceria-based electrolyte, *Nanomaterials* 11 (2021) 2231, <https://doi.org/10.3390/nano11092231>.

[55] M. Li, B. Hua, J. Luo, S.P. Jiang, J. Pu, B. Chi, J. Li, Enhancing sulfur tolerance of Ni-based cermet anodes of solid oxide fuel cells by ytterbium-doped barium cerate infiltration, *ACS Appl. Mater. Interfaces* 8 (2016) 10293–10301, <https://doi.org/10.1021/acsami.6b00925>.

[56] M. Piutti, S. Bensaid, N. Russo, D. Fino, Nanostructured ceria-based catalysts for soot combustion: Investigations on the surface sensitivity, *Appl. Catal. B* 165 (2015) 742–751, <https://doi.org/10.1016/j.apcatb.2014.10.062>.

[57] J. Zhang, F. Wei, Z. Yang, Q. Chen, J. Chen, S. Wang, Structure and chemical states of highly epitaxial CeO₂(001) films grown on SrTiO₃ substrate by laser molecular beam epitaxy, *J. Rare Earths* 31 (2013) 1191–1194, [https://doi.org/10.1016/S1002-0721\(12\)60425-6](https://doi.org/10.1016/S1002-0721(12)60425-6).

[58] L. Li, B. Zhu, J. Zhang, C. Yan, Y. Wu, Electrical properties of nanocube CeO₂ in advanced solid oxide fuel cells, *Int. J. Hydron. Energy* 43 (2018) 12909–12916, <https://doi.org/10.1016/j.ijhydene.2018.05.120>.

[59] M.Z. Khan, M.T. Mehran, R.-H. Song, J.-W. Lee, S.-B. Lee, T.-H. Lim, A simplified approach to predict performance degradation of a solid oxide fuel cell anode, *J. Power Sources* 391 (2018) 94–105, <https://doi.org/10.1016/j.jpowsour.2018.04.080>.

[60] M. Siebenhofer, C. Riedl, A. Schmid, A. Limbeck, A.K. Opitz, J. Fleig, M. Kubicek, Investigating oxygen reduction pathways on pristine SOFC cathode surfaces by: in situ PLD impedance spectroscopy, *J. Mater. Chem. A Mater. Interfaces* 10 (2022), <https://doi.org/10.1039/dta07128a>.

[61] M.Z. Khan, R.-H. Song, A. Hussain, S.-B. Lee, T.-H. Lim, J.-E. Hong, Effect of applied current density on the degradation behavior of anode-supported flat-tubular solid oxide fuel cells, *J. Eur. Ceram. Soc.* 40 (2020) 1407–1417, <https://doi.org/10.1016/j.jeurceramsoc.2019.11.017>.

[62] J.D. Nicholas, L. Wang, A.V. Call, S.A. Barnett, Use of the simple infiltrated microstructure polarization loss estimation (SIMPLE) model to describe the performance of nano-composite solid oxide fuel cell cathodes, *Phys. Chem. Chem. Phys.* 14 (2012), <https://doi.org/10.1039/c2cp43370b>.

[63] S.W. Baek, J. Bae, Y.S. Yoo, Cathode reaction mechanism of porous-structured Sm_{0.5}Sr_{0.5}CoO₃-δ and Sm_{0.5}Sr_{0.5}CoO₃-δ/N₂O₂Ce_{0.8}O_{1.9} for solid oxide fuel cells, *J. Power Sources* 193 (2009) 431–440, <https://doi.org/10.1016/j.jpowsour.2009.03.071>.

[64] M. Choi, J. Lee, W. Lee, Nano-film coated cathode functional layers towards high performance solid oxide fuel cells, *J. Mater. Chem. A Mater. Interfaces* 6 (2018), <https://doi.org/10.1039/c8ta01660g>.

[65] C. Sun, R. Hui, J. Roller, Cathode materials for solid oxide fuel cells: a review, *J. Solid State Electrochem.* 14 (2010), <https://doi.org/10.1007/s10008-009-0932-0>.

[66] C. Endler-Schuck, J. Joos, C. Niedrig, A. Weber, E. Ivers-Tiffée, The chemical oxygen surface exchange and bulk diffusion coefficient determined by impedance spectroscopy of porous La_{0.58}Sr_{0.4}Co_{0.2}Fe_{0.8}O₃ – δ (LSCF) cathodes, *Solid State Ion.* 269 (2015) 67–79, <https://doi.org/10.1016/j.ssi.2014.11.018>.

[67] J.D. Kim, G.D. Kim, J.W. Moon, Y. il Park, W.H. Lee, K. Kobayashi, M. Nagai, C. E. Kim, Characterization of LSM-YSZ composite electrode by ac impedance spectroscopy, *Solid State Ion.* 143 (2001), [https://doi.org/10.1016/S0167-2738\(01\)00877-3](https://doi.org/10.1016/S0167-2738(01)00877-3).

[68] S. Mulmi, V. Thangadurai, A perovskite-type Nd_{0.75}Sr_{0.25}Co_{0.8}Fe_{0.2}O₃-δ cathode for advanced solid oxide fuel cells, *Chem. Commun.* 55 (2019), <https://doi.org/10.1039/c9cc01054h>.

[69] H.-N. Im, M.-B. Choi, B. Singh, D.-K. Lim, S.-J. Song, Investigation of oxygen reduction reaction on La 0.1 Sr 0.9 Co 0.8 Fe 0.2 O 3- δ electrode by electrochemical impedance spectroscopy, *J. Electrochim. Soc.* 162 (2015), <https://doi.org/10.1149/2.0581507jes>.

[70] F. Zhong, Z. Li, Y. Luo, C. Chen, C. Zhou, L. Lin, G. Cai, C. Au, L. Jiang, Geometric structure distribution and oxidation state demand of cations in spinel Ni_xFe_{1-x}Co₂O₄ composite cathodes for solid oxide fuel cells, *Chem. Eng. J.* 425 (2021), <https://doi.org/10.1016/j.cej.2021.131822>.

[71] M. Li, Z. Sun, W. Yang, T. Hong, Z. Zhu, Y. Zhang, X. Wu, C. Xia, Mechanism for the enhanced oxygen reduction reaction of La_{0.6}Sr_{0.4}Co_{0.2}Fe_{0.8}O_{3- δ} by strontium carbonate, *Phys. Chem. Chem. Phys.* 19 (2017), <https://doi.org/10.1039/c6cp06204k>.

[72] I. Thaheem, K.J. Kim, J.J. Lee, D.W. Joh, I. Jeong, K.T. Lee, High performance Mn_{1.3}Co_{1.3}Cu_{0.4}O₄ spinel based composite cathodes for intermediate temperature solid oxide fuel cells, *J. Mater. Chem. A Mater.* 7 (2019), <https://doi.org/10.1039/c9ta07069a>.

[73] Z. Duan, M. Yang, A. Yan, Z. Hou, Y. Dong, Y. Chong, M. Cheng, W. Yang, Ba_{0.5}Sr_{0.5}Co_{0.8}Fe_{0.2}O_{3- δ} as a cathode for IT-SOFCs with a GDC interlayer, *J. Power Sources* 160 (2006), <https://doi.org/10.1016/j.jpowsour.2006.01.092>.

[74] S.P. Jiang, X. Chen, Chromium deposition and poisoning of cathodes of solid oxide fuel cells – a review, *Int. J. Hydrog. Energy* 39 (2014) 505–531, <https://doi.org/10.1016/j.ijhydene.2013.10.042>.

[75] Z. Cheng, H. Abernathy, M. Liu, Raman spectroscopy of nickel sulfide Ni₃S₂, *J. Phys. Chem. C* 111 (2007), <https://doi.org/10.1021/jp0770209>.

[76] Z. Cheng, J.H. Wang, Y. Choi, L. Yang, M.C. Lin, M. Liu, From Ni-YSZ to sulfur-tolerant anode materials for SOFCs: electrochemical behavior, in situ characterization, modeling, and future perspectives, *Energy Environ. Sci.* 4 (2011), <https://doi.org/10.1039/clee01758f>.

[77] N.E. Marotta, J.R. Barber, P.R. Dluffy, L.A. Bottomley, Patterned silver nanorod array substrates for surface-enhanced Raman scattering, *Appl. Spectrosc.* 63 (2009), <https://doi.org/10.1366/000370209789553174>.

[78] J.M. McLellan, A. Siekkinen, J. Chen, Y. Xia, Comparison of the surface-enhanced Raman scattering on sharp and truncated silver nanocubes, *Chem. Phys. Lett.* 427 (2006), <https://doi.org/10.1016/j.cplett.2006.05.111>.

[79] X. Li, K. Blinn, D. Chen, M. Liu, In situ and surface-enhanced raman spectroscopy study of electrode materials in solid oxide fuel cells, *Electrochim. Energy Rev.* 1 (2018), <https://doi.org/10.1007/s41918-018-0017-9>.

[80] B. Wei, K. Chen, L. Zhao, Z. Lü, S. Ping Jiang, Chromium deposition and poisoning at La 0.6 Sr 0.4 Co 0.2 Fe 0.8 O 3- δ oxygen electrodes of solid oxide electrolysis cells, *Phys. Chem. Chem. Phys.* 17 (2015) 1601–1609, <https://doi.org/10.1039/C4CP05110F>.

[81] J.J. Bentzen, J.V.T. Hågh, R. Barfod, A. Hagen, Chromium poisoning of LSM/YSZ and LSCE/CGO composite cathodes, *Fuel Cells* 9 (2009) 823–832, <https://doi.org/10.1002/fuce.200800143>.

[82] M.Z. Khan, R.H. Song, M.T. Mehran, S.B. Lee, T.H. Lim, Controlling cation migration and inter-diffusion across cathode/interlayer/electrolyte interfaces of solid oxide fuel cells: a review, *Ceram. Int.* 47 (2021) 5839–5869, <https://doi.org/10.1016/J.CERAMINT.2020.11.002>.

[83] Y.L. Huang, A.M. Hussain, C. Pellegrinelli, C. Xiong, E.D. Wachsman, Chromium poisoning effects on surface exchange kinetics of La_{0.6}Sr_{0.4}Co_{0.2}Fe_{0.8}O_{3- δ} , *ACS Appl. Mater. Interfaces* 9 (2017) <https://doi.org/10.1021/acsmami.7b02762>.

[84] W. Lee, J.W. Han, Y. Chen, Z. Cai, B. Yıldız, Cation size mismatch and charge interactions drive dopant segregation at the surfaces of manganite perovskites, *J. Am. Chem. Soc.* 135 (2013) 7909–7925, <https://doi.org/10.1021/ja3125349>.

[85] D.S. Mebane, A variational approach to surface cation segregation in mixed conducting perovskites, *Comput. Mater. Sci.* 103 (2015), <https://doi.org/10.1016/j.commatsci.2014.11.025>.

[86] H. Ding, A.V. Virkar, M. Liu, F. Liu, Suppression of Sr surface segregation in La_{1-x}Sr_xCo_{1-y}Fe_yO_{3- δ} : a first principles study, *Phys. Chem. Chem. Phys.* 15 (2013).

[87] S.U. Rehman, H.-S. Song, H.-S. Kim, M. Haseeb Hassan, D.-W. Joh, R.-H. Song, T.-H. Lim, J.-E. Hong, S.-J. Park, S.-B. Lee, A dynamic infiltration technique to synthesize nanolayered cathodes for high performance and robust solid oxide fuel cells, *J. Energy Chem.* 70 (2022) 201–210, <https://doi.org/10.1016/j.jechem.2022.02.052>.

[88] Y.H. Song, S.U. Rehman, H.S. Kim, H.S. Song, R.H. Song, T.H. Lim, J.E. Hong, S. J. Park, J.Y. Huh, S.B. Lee, Facile surface modification of LSCF/GDC cathodes by epitaxial deposition of Sm_{0.5}Sr_{0.5}Co_{0.3}O₃ via ultrasonic spray infiltration, *J. Mater. Chem. A Mater.* 8 (2020) 3967–3977, <https://doi.org/10.1039/c9ta11704k>.

[89] Y. Chen, S. Yoo, X. Li, D. Ding, K. Pei, D. Chen, Y. Ding, B. Zhao, R. Murphy, B. deGlee, J. Liu, M. Liu, An effective strategy to enhancing tolerance to contaminants poisoning of solid oxide fuel cell cathodes, *Nano Energy* 47 (2018), <https://doi.org/10.1016/j.nanoen.2018.03.043>.

[90] Y. Niu, Y. Zhou, W. Lv, Y. Chen, Y. Zhang, W. Zhang, Z. Luo, N. Kane, Y. Ding, L. Soule, Y. Liu, W. He, M. Liu, Enhancing oxygen reduction activity and Cr tolerance of solid oxide fuel cell cathodes by a multiphase catalyst coating, *Adv. Funct. Mater.* (2021), <https://doi.org/10.1002/adfm.202100034>.

[91] K. Pei, Y. Zhou, K. Xu, Z. He, Y. Chen, W. Zhang, S. Yoo, B. Zhao, W. Yuan, M. Liu, Y. Chen, Enhanced Cr-tolerance of an SOFC cathode by an efficient electro-catalyst coating, *Nano Energy* 72 (2020), <https://doi.org/10.1016/j.nanoen.2020.104704>.

[92] K. Chen, N. Ai, K.M. O'Donnell, S.P. Jiang, Highly chromium contaminant tolerant BaO infiltrated La 0.6 Sr 0.4 Co 0.2 Fe 0.8 O 3- δ cathodes for solid oxide fuel cells, *Phys. Chem. Chem. Phys.* 17 (2015), <https://doi.org/10.1039/c4cp04172k>.